Ph.D. DISSERTATION

# Disorder engineering and localization control in planar multilayer film

## 평면 다층 필름의 무질서 설계 및 파동 국부화 제어

BY

OH SEUNGHWA

AUGUST 2022

DEPARTMENT OF ELECTRICAL AND
COMPUTER ENGINEERING
COLLEGE OF ENGINEERING
SEOUL NATIONAL UNIVERSITY

Ph.D. DISSERTATION

# Disorder engineering and localization control in planar multilayer film

## 평면 다층 필름의 무질서 설계 및 파동 국부화 제어

BY

OH SEUNGHWA

AUGUST 2022

DEPARTMENT OF ELECTRICAL AND
COMPUTER ENGINEERING
COLLEGE OF ENGINEERING
SEOUL NATIONAL UNIVERSITY

# Disorder engineering and localization control in planar multilayer film

평면 다층 필름의 무질서 설계 및 파동 국부화 제어

지도교수 박 남 규
이 논문을 공학박사 학위논문으로 제출함

2022년 8월

서울대학교 대학원

전기 · 정보 공학부

오 승 화

오승화의 공학박사 학위 논문을 인준함

2022년 8월

| | | |
|---|---|---|
| 위 원 장: | 정 윤 찬 | (인) |
| 부위원장: | 박 남 규 | (인) |
| 위 원: | 김 기 홍 | (인) |
| 위 원: | 오 정 석 | (인) |
| 위 원: | 유 선 규 | (인) |

# Abstract

## Disorder engineering and localization control in planar multilayer film

OH SEUNGHWA
DEPARTMENT OF ELECTRICAL AND
COMPUTER ENGINEERING
COLLEGE OF ENGINEERING
SEOUL NATIONAL UNIVERSITY

The wave phenomena in a disordered material have been of great interest since Anderson discovered the absence of diffusion in disordered crystals. In disordered photonics, recent research focuses on wave localization and diffusion in subwavelength structures and the controlled correlation length for the wave transport in disordered media. Corresponding results of wave-disorder interactions in perturbed periodic systems and targeting controllable subwavelength interactions and unconventional optical properties have been made in

engineered disorder. Therefore, the need for disorder engineering is understandable as proper structural correlation manipulation enables handling multiple physical quantities such as spectral responses, transport and localization, angular responses, and topological properties.

In the matter of the disorder scale, intriguing recent achievements show the emergence of strong localization induced by the accumulated Goos–Hänchen phase shifts, which leads to the breakdown of the Effective Medium Theory, and the appearance of abnormal transmission over the critical angle. However, a deeper understanding of the connection between underlying physical phenomena of Goos–Hänchen phase accumulation, spatial order metric, and wave phenomena is still absent, hindering a higher-level abstraction or application such as the inverse design deep-subwavelength disorder structure with the target designer interactions.

In this dissertation, I demonstrate deep-subwavelength disorder planar multilayer films engineered with target order metric $\tau$. Then, I provide the correlation between the order metric $\tau$ and the abnormal behavior of disorder-induced transmission and localization length, proving the possible applications of the disorder engineering in the control of localization and optical properties - including localization, transport, and spectral-/angular- responses. The correla-

tion between the thickness disorder of the films and the locations of localization hubs is also discussed. These localization hubs create an additional wave propagation path for an enhanced lateral displacement, auxiliary Goos–Hänchen shift, on the reflecting side. Additionally, by applying symmetry to disorder, laterally shifted wave transmission is found for the first time.

This dissertation is expected to provide a deeper understanding of wave-disorder interaction and promising disorder engineering applications to control abnormal optical characteristics around the critical angle by controlling localization hubs. Significantly, the emergence and enhancement of the auxiliary Goos–Hänchen shift and transmission shift enlighten a new perspective on the potential application in angular filter and sensing.

**keywords**: Disorder engineering, Deep-subwavelength disorder, Disorder-induced localization control, Localization hub, Auxiliary Goos–Hänchen shift, Transmission shift

**student number**: 2018-37775

# Contents

# List of Figures

# Chapter 1

# INTRODUCTION

In this chapter, I overview the previous studies and challenges in disordered media. I introduce disorder-induced transport, localization, and abnormal optical responses related to the subwavelength disorder. The fundamental challenge underlying understanding the connection between wave phenomena and disorder is discussed. In the last section, the outline of this dissertation is described.

## 1.1 Previous studies and challenges in disordered media

Disorder can describe every kind of irregularity in spatial distributions. Mostly, disorder is used for describing fully random systems. However, considering the grey area between two extremes, disorder can be defined over a large area to

be explored, thus having high potential. Research in disorder photonics started with the localization of light in disordered crystals, uncorrelated disorder, by Anderson [1]. Since then, the research on disordered photonics has focused on studying wave localization and diffusion in subwavelength structures [2][3] and investigating the controlled correlation length for wave transport in disordered media [4]. These efforts have produced unconventional wave behaviors distinct from diffusive transport [5] and weak [6] or strong [1] localization - such as the branched flow of light [4], supporting longer correlation lengths than the wavelength of light. Though currently incomplete, the quest to reveal the hidden relations between the disorder metrics, characteristic lengths, and various wave properties constitutes the essential core in the understanding and application of disordered systems.

Wave in disordered media experiences complex interactions inherited by disorder, and the same degree of disorder does not always elicit the same wave response. In order to obtain desirable wave phenomena, the engineered disorder should be considered. As summarized in a recent review article [7], the proper manipulation of structural correlation enables the handling of multiple physical quantities, such as spectral responses, transport and localization, angular responses, and topological properties. The developments in hyperuniformity [8][9][10][11][12] have clarified the role of structural correlation in reciprocal

space, achieving isotropic photonic bandgaps [13][14][15] and almost perfect transparency [16].

On the other hand, with recent achievements in deep subwavelength disorder (DSD) [2][3], it has become sensible to consider the inverse engineering of DSD. For this purpose, considering the peculiarities in the extreme regime of DSD, such as the breakdown of effective medium theory (EMT) and the associated emergence of the strong localization induced by the accumulated Goos–Hänchen phase shifts [4], there exists a need to reveal the unconventional phenomena of modal localization around the critical angle in relation to the spatial disorder. For example, the abnormal optical responses above the critical angle for noncrystalline "order" with their specific long-range correlations have been studied [17][18] concerning applications in angle-selective filtering and stronger energy concentration.

## 1.2 Outline of the dissertation

This dissertation focuses on the abnormal wave phenomena induced by disorder, such as the localization length, transmission, and Goos–Hänchen shift (GHS), caused by the disorder design oriented to the order metric. In chapter 2, I briefly introduce the structure of planar dichromic multilayer films. Then

I provide the definition of the order metric $\tau$ and the target-oriented inverse engineering method. In chapter 3, the simulation result of disordered films is discussed. The abnormal optical responses in the localization length and transmission are presented, and the emergence and the enhancement of the auxiliary GHS are addressed. The presented auxiliary GHS gives a new perspective on GHS engineering using deep-subwavelength disorder within the multilayer films. The simulation setup in this work is also mentioned here. Chapter 4 presents the newly proposed transmission shift using symmetric disorder. The mirror-folding symmetry is applied to the disordered film, and the laterally shifted transmission is found for the first time.

# Chapter 2

# ENGINEERED DEEP-SUBWAVELENGTH DISORDER

This chapter introduces the design method of disordered multilayer films of the deep-subwavelength scale. First, I briefly provide common structural characteristics of multilayer films. Finally, the $\tau$ order metric-based design of disordered films is described, including the definition of the order metric $\tau$. The advantage of using $\tau$ order metric engineering is also discussed.

## 2.1 Planar dichromic multilayer film

We consider a planar dichromic multilayer film sandwiched between a pair of homogeneous dielectrics with the relative permittivity $\epsilon_{clad} = 4$ as in Fig. 2.1 (The transition of the spatial distribution to the structural factor, the bottom side of Fig. 2.1 will be discussed in Section 2.2.1). The multilayer film consists

of $N = 200$ pairs of alternating layers of low ($\epsilon_L = 1$) and high ($\epsilon_H = 5$) relative permittivity with thicknesses of $d_{L,q}$ and $d_{H,q}$, respectively, where $q$ is the index of the layer ($1 \leq q \leq N$) and $d_{L,q} = d_{H,q} = 20\ nm$ for the periodic multilayer film. The perturbed thickness distribution ranges between $0 \sim 40\ nm$, and the number of alternative layers is kept the same, and the spatial fill factor $f$, which is the same as the volume fraction of $\epsilon_L$ and $\epsilon_H$ for the whole film, is set to be identical ($f = 0.5$), leading to fixed effective permittivity $\epsilon_{eff} = (\epsilon_L + \epsilon_H)/2 = 3$ for both periodic and disordered films.

## 2.2 Engineered disorder

### 2.2.1 Order metric $\tau$

To address the degree of order of the suggested platform, I apply the translational order metric $\tau$ originally introduced by Torquato [19]. Specifically, I employ the discrete-space version of the $\tau$ metric because our structure is pixelized to two-phase heterogeneous media, similar to [20]. The order metric $\tau$ defined in [20] measures the statistical deviation of a given disordered film compared to the uncorrelated disorder with a Poisson distribution. For the derivation of the order metric $\tau$ in planar dichromic multilayer films, I calculate the static structure factor $S(k)$ in reciprocal space [21] by introducing the

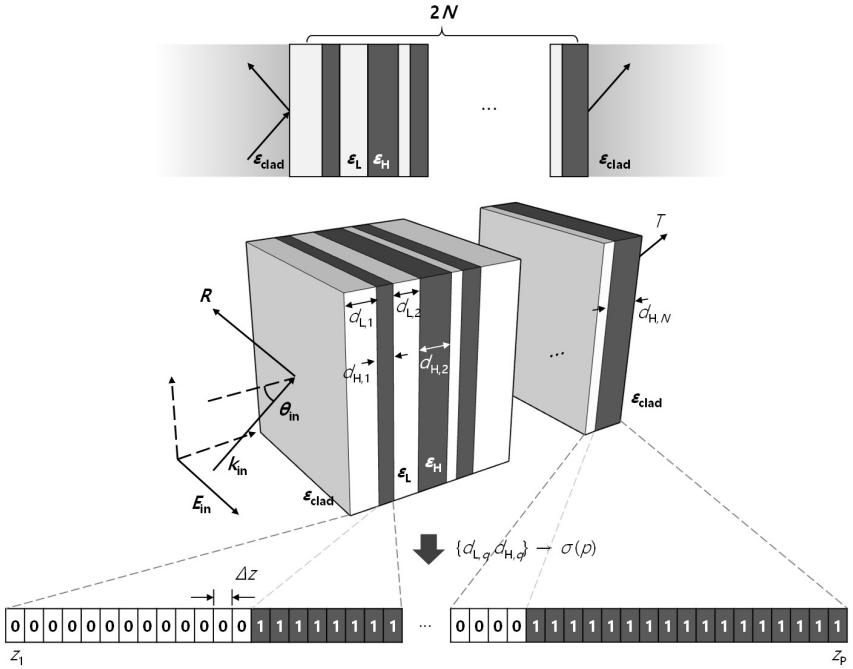


Figure 2.1: A schematic of a planar deep-subwavelength disordered multilayer film and the process of converting the thicknesses $\{d_{L,q}, d_{H,q}\}$ to the indicator function $\sigma(p)$. The disordered film consists of layers of varying thicknesses of two alternating materials. $d_{L,q}$, and $d_{H,q}$ denote the thicknesses of the $\epsilon_L$ layer and $\epsilon_H$ layer at $q$, respectively ($1 \leq q \leq N$). We analyze the effect of disordered profiles on the optical responses (transmittance, characteristic length, and reflection coefficient) to oblique incidence (incidence angle $\theta_{in}$). $E_{in}$ represents the direction of the input electric polarization.

discretized spatial coordinate $z_p$ (integer $p \in [1, P]$) with the uniform grid size $\Delta z$. The total thickness of the heterogeneous film is fixed at $L$ ($L = P\Delta z$, in the current case, $L = 8\ \mu m$ with $P = 80,000$ and $\Delta z = 0.1\ nm$), and at each $z_p$ ($\Delta z/2 \leq z_p \leq L - \Delta z/2$), I define the indicator function $\sigma(p)$ with a binary output $\sigma(p) = 0$ for the $\epsilon_L$ layer and $\sigma(p) = 1$ for the $\epsilon_H$ layer (see Fig. 2.1 Bottom). The $\epsilon_H$ layer is considered a particle in the point process of $S(k)$. The static structure factor $S(k)$ is then given by:

$$S(k) = \frac{1}{\sigma_H} \left| \sum_{p=1}^{P} \sigma(p) e^{ikp} \right|^2 \tag{2.1}$$

where $\sigma_H = \Sigma\sigma(p) = P/2$ is the number of $\epsilon_H$ sites. The $\tau$ order metric then becomes

$$\tau = \sum_{k \neq 0} \left[ S(k) - S_p(k) \right]^2 = \sum_{k \neq 0} \left[ S(k) - (1 - f) \right]^2 \tag{2.2}$$

where $S_p(k) = 1 - f = 0.5$ is the structure factor of the uncorrelated structure obtained from the Poisson point process [9]. As $\tau$ denotes the deviation from the uncorrelated structure ($\tau = 0$ with $S(k) = 0.5$ for all $k \neq 0$), the maximum value of $\tau = 1$ is that of the periodic film $\tau_p$. Normalizing the calculated $\tau$ of the disordered film to the $\tau_p$ of the periodic film, thus $\tau \in [0, 1]$, which I use hereafter.

### 2.2.2 $\tau$-oriented inverse engineering

To prepare an ensemble of multilayer films achieving the same target order metric $\tau$ with distinct disordered spatial configurations, I employ the Metropolis algorithm, which is known to provide an inversely designed canonical ensemble in a stable and straightforward manner [22]. The flowchart for the inverse design process is shown in Fig. 2.2. The initial multilayer film is a periodic film ($\tau_{initial} = 1$) consisting of $N(200)$ pairs ($\epsilon_L, \epsilon_H$), with $d_{L,q} = d_{H,q} = 20\ nm$. To achieve a multilayer film with a targeted order metric, $\tau_{target}$, I introduce disorder to the thicknesses of the multilayer film. For the ease of thickness control, I define a thickness matrix $D$ (and perturbation matrix $\Delta D$) of size $N \times 2$ with $d_{L,q}$ and $d_{H,q}$ as the matrix components at each column representing $\epsilon_L$ and $\epsilon_H$ (see Fig. 2.2). Each column of $\Delta D$, i. e., $\Delta D_L(\{\Delta d_{L,q}\})$ or $\Delta D_H(\{\Delta d_{H,q}\})$, having normal distribution is then generated while keeping $|\Sigma \Delta D_L|$ and $|\Sigma \Delta D_L| < 0.001\ nm$ and the number of $(\epsilon_L, \epsilon_H)$ pairs $N = 200$ to maintain the total film thickness as well the spatial fill factor $f = 0.5$. It is noted that while the continuous perturbation of the thickness could affect the domain size of the simulation space, we suppress its effect on the $\tau$ order metric by imposing the restriction of $|\Sigma \Delta D_{L,H}| < 0.001\ nm$ in the inverse design process. Therefore, our work can be considered the inclusion of $\epsilon_H$ particles inside the $\epsilon_L$ domain (or vice versa), preserving the simulation space, or

equivalently the total film thickness.

After $\sigma(p)$ and $\tau$ are updated with $D' = D + \Delta D$, the deviation of $\tau$ to $\tau_{target}(\Delta\tau = \tau - \tau_{target})$ is calculated, and the process is repeated until $\Delta\tau < 0.1\tau_{target}$. In Fig. 2.3, the example of the iterative $\tau$ evaluation is depicted in time wise domain. The final output of the Metropolis algorithm then becomes $D_{final}$ for the disordered multilayer film of $\tau_{target}$, with 200 pairs of layer thicknesses $d_{L,q}$, and $d_{H,q}$. Care must be taken to optimize the distribution of $\Delta D$ because a variation that is too large leads to a penalty in precision. The standard deviation of $\Delta D_L$ or $\Delta D_H$ is set to be $\Delta\tau$ dependent, $0.25\ nm$ when $|\Delta\tau| < 0.05$ and $0.5\ nm$ otherwise, to optimize both the computation time and precision.

The success rate of multilayer film generation for a given $\tau_{target}$ is over $83\%$ out of 3,000 realizations, confirming the stability of the inverse design process. The obtained relationship between $\tau_{target}$ and the distribution of the multilayer film thicknesses is shown in Fig. 2.4. As $\tau_{target}$ decreases ($\tau_{target} = 0.5, 0.1, 0.02$, and $0.01$), the thickness distribution disperses as expected. If the normal distribution, which only varies in standard deviation, is applied instead of the algorithm above, obtaining $\tau$ in a certain range is impossible, thus supporting the fairness of using $\tau$-based engineered disorder. The variation in the critical angle using the effective permittivity $\theta_c = sin^{-1}((\epsilon_{eff}/\epsilon_{clad})^{\frac{1}{2}})$, where

$\epsilon_{eff} = (\epsilon_L + \epsilon_H)/2 = 3$, is within $3 \times 10^{-4}$ degrees for all realizations, confirming that all realizations are equal in the EMT sense. It is worth to note that our design approach of applying the normal-distribution perturbation to the layer thickness corresponds to the systematic perturbation of lattice structures, leading to Gaussian-perturbed lattices. In view of a much larger space of material phases offered by disorder, our method thus covers a specific subspace in the material phase: including both short-range and long-range density fluctuations while preserving a significant amount of long-range periodic order [23]. While the variety of material phases is assured in our implementation guaranteed by the target order metric $\tau$ between 0 (Random) and 1 (Periodic), the extension of the study for different material phase spaces would be possible, for example, by varying the probability density function in the perturbation which is currently the normal distribution, or utilizing other models that provide highly correlated yet disordered landscape without Bragg peaks.

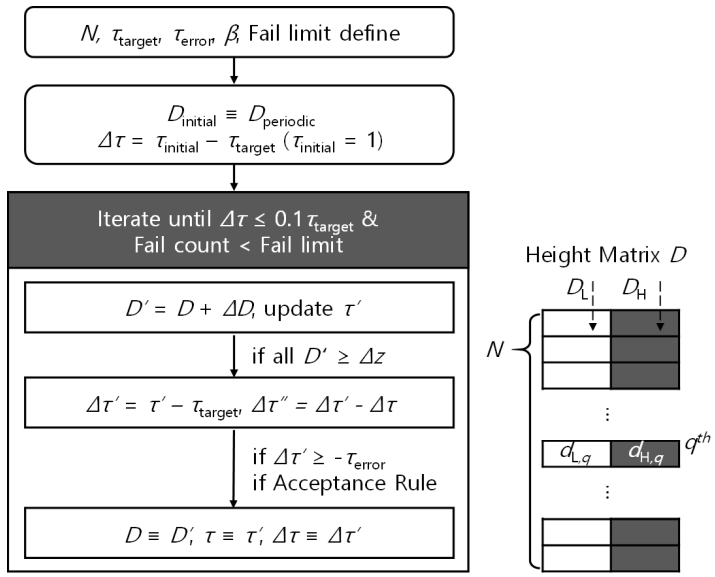


Figure 2.2: A flowchart of the entire disorder engineering process is illustrated, including the iterative steps of creating and adding the thickness variation $\Delta D$ to the initial thickness $D_{periodic}$ toward the $D_{final}$ of $\tau_{target}$.

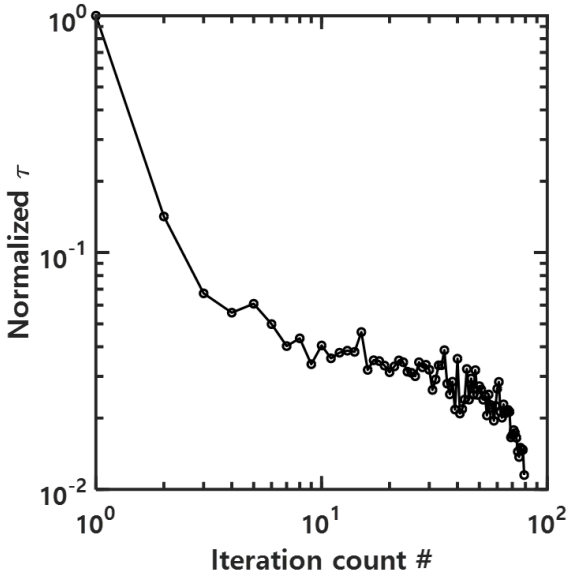


Figure 2.3: The variation of the normalized $\tau$ of a single disorder realization, as an example of the iterative process. It is obvious that the $\Delta\tau$ dependent standard deviation is effective in reducing computation time, and $\tau_{target} = 0.01$ is met in less than 100 loops.

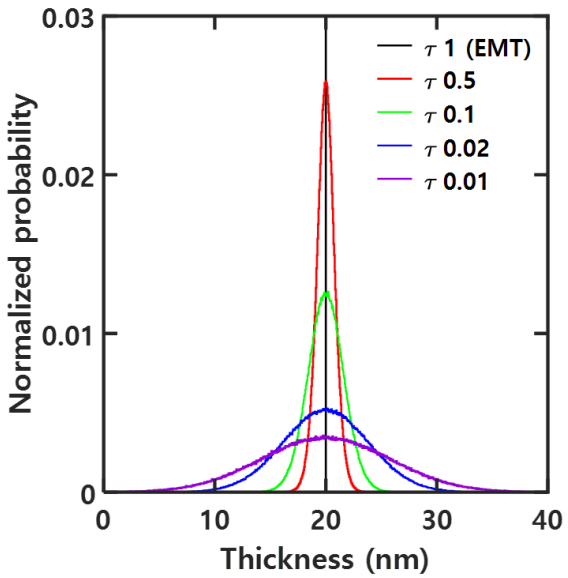


Figure 2.4: The normalized probability distribution of the film thickness in the ensemble of the identical $\tau_{target}$. As $\tau_{target}$ decreases from 0.5 to 0.01, the thickness variation increases as the film structure tends toward more uncorrelated disordered systems.

# Chapter 3

# DISORDER-INDUCED ABNORMAL OPTICAL RESPONSES

This chapter discusses the abnormal optical responses caused by disorder, in disordered films, considering transverse electric (TE) polarized plane wave incidences with the incidence angle $\theta_{in}$ and the free-space wavelength $\lambda_0 = 1\ \mu m$. First, I provide the disorder-induced abnormal phenomena of the localization length and the transmission around the critical angle. The matching with the previously studied analytic solution assists the understanding of the abnormal phenomena. I also present the scale dependency of disorder in the manner of the disorder-induced optical responses, which supports the importance of applying deep-subwavelength scale disorder. Finally, the emergence and enhancement of an auxiliary GHS are introduced with the concept of localization

hubs. The conventional GHS and its tuning are achieved by using the resonance at a dielectric/dielectric or metal/dielectric interface [24][25][26][27][28] or by introducing defect states within the structure [29]. The newly found auxiliary GHS has an important difference from the conventional GHS in the enhancement of lateral shift length and the basic formation principle. I also discuss the example of the auxiliary GHS tuning compared to the previous perspective on GHS engineering.

## 3.1 Localization length and Transmission

For planar DSD films near the critical angle $\theta_c$, there exists an abnormality [30] deviating from the EMT due to the differences in a phase accumulation arising from DSD. When the thickness variation of the layers is on a deep subwavelength scale, in addition to the phase accumulation from the propagation delay, the phase accumulation through Fresnel reflection, a.k.a. the Goos–Hänchen phase shift, starts to contribute. Sheinfux [2] studied the case of a planar film with uncorrelated disorder focusing on the abnormal transmission around $\theta_c$, identifying two different regimes of TE incident angle according to the wave behavior inside the layers. The two characteristic critical angles are given by $\theta_L = sin^{-1}((\epsilon_L/\epsilon_{clad})^{\frac{1}{2}})$ and $\theta_c = sin^{-1}((\epsilon_{eff}/\epsilon_{clad})^{\frac{1}{2}})$ for the per-

mittivity of the cladding material $\epsilon_{clad}$. The regime of $\theta_L < \theta < \theta_c$ is called the Goos–Hänchen localization (GHL) regime, as the translation phase accumulation achieved by Fresnel reflection induces localization in this regime. The regime of $\theta_c < \theta$ is defined as the effective medium evanescence (EME) regime, as the overall transmittance decays exponentially. In this interesting regime, a narrower-bandwidth localization with a higher quality factor Q also appears, which is the main reason for the "abnormal" narrowband transmission enhancement in the EME regime, where the exponential decay of the transmission is natural.

Considering that this abnormal transmission in the EME regime is attributed to the overwhelming localization in the subwavelength disordered structure [2], improving the abnormal transmission in the EME regime should be possible by proactively engineering the degree of disorder. For the inversely designed DSD film ensembles, 3,000 realizations of each $\tau_{target}$ using the Metropolis algorithm and the optical responses (transmission and reflection at incident angles between $0^\circ$ and $66^\circ$) are analyzed using the transfer matrix method (TMM). Most importantly, I numerically calculated the wave-localization length at each $\tau_{target}$ with $\xi^{-1} = -\langle lnT \rangle / L$ [31] by taking the ensemble average over the group of realizations at a given $\tau_{target}$, where $T$ is the transmission of each realization and $L$ is the thickness of the multilayer film. For comparison with the

numerical result, the analytical calculation of the localization length $\xi$ is carried out assuming the same permittivity realization following the procedures in [32]. This has not been tested for DSD structures or the Goos–Hänchen translational phase shift for its validity.

In detail, the disordered multilayer films in [32] are assumed to be an inhomogeneous slab of $\epsilon(z) = \epsilon_{eff} + \delta\epsilon(z)$, where $\epsilon_{eff} = \langle\epsilon(z)\rangle$ and $\langle\delta\epsilon(z)\rangle = 0$ ($0 \leq z \leq L$). With a cladding of $\epsilon_{clad}$ and an obliquely impinging s-polarized plane wave where $k^2 = \epsilon_E k_0^2$, the complex amplitude of the electric field $\boldsymbol{E}$ inside the media becomes

$$\begin{aligned} &\frac{\partial^2 E}{\partial z^2} + \left[k_0^2\epsilon(z) - k^2 sin^2\theta_{in}\right] E = \\ &\frac{\partial^2 E}{\partial z^2} + (k cos\theta_{in})^2 \left[1 + \frac{\frac{\epsilon_{eff}}{\epsilon_{clad}} - 1 + \frac{\delta\epsilon(z)}{\epsilon_{clad}}}{cos^2\theta_{in}}\right] E = 0 \end{aligned} \tag{3.1}$$

For the random distribution of the present permittivity profile, I adopt a short-range correlation model in [33] with the correlation length $l_c$

$$\langle\delta\tilde{\epsilon}(z)\delta\tilde{\epsilon}(z')\rangle = \rho^2 exp(-|z - z'|/l_c),\ \langle\delta\tilde{\epsilon}(z)\rangle = 0 \tag{3.2}$$

where a random variable $\delta\tilde{\epsilon}(z) = \delta\epsilon(z)/\epsilon_{clad}$, which is further reduced to

$$\langle\delta\tilde{\epsilon}(z)\delta\tilde{\epsilon}(z')\rangle = 2g_0\delta(z - z'),\ \langle\delta\tilde{\epsilon}(z)\rangle = 0 \tag{3.3}$$

in the case of $\rho \to \infty$, $l_c \to 0$ and $\rho^2 l_c \to g_0$, where $g_0$ is the strength of disorder. On the other hand, the Schrödinger equation for a quantum-mechanical particle in a random potential $V(z)$ in one dimension can be written as,

$$\frac{\partial^2 \Psi}{\partial z^2} + \kappa^2 \left[1 - \frac{V(z)}{E}\right] \Psi = 0 \tag{3.4}$$

where $\boldsymbol{E}$ is the energy of the incoming particle and the potential $V(z)$ is $V_0 + \delta V(z)$ for $0 \leq z \leq L$ and 0 for $z < 0$ and $z > L$. The average potential is $V_0$ and is a random function $\delta V(z)$ satisfies $\langle \delta V(z) \rangle = 0$.

$$\langle \delta V(z) \delta V(z') \rangle = 2D\delta(z - z'),\ \langle \delta V(z) \rangle = 0 \tag{3.5}$$

These two equations have a duality relation between electric field in the random permittivity profile and the quantum-mechanical particle in a random potential. In the case of the transmission of a quantum particle through the random potential, the Lyapunov exponent $\gamma$ is defined as

$$\lim_{x \to \infty} \frac{\langle lnT \rangle}{2L} = -\gamma \tag{3.6}$$

As $\gamma$ can be related to the localization length $\xi$ by $\gamma = 1/2\xi$, $\gamma$ is [34]

$$\gamma = \left(\frac{\kappa^4 D}{E^2}\right) F\left(\left(\frac{E^2}{\kappa D}\right)^{\frac{2}{3}}\left(\frac{V_0}{E} - 1\right)\right) \tag{3.7}$$

where F(X) is expressed in the Airy functions and their derivatives

$$F(X) = \frac{Ai(X)Ai'(X) + Bi(X)Bi'(X)}{\left[Ai(X)\right]^2 + \left[Bi(X)\right]^2} \tag{3.8}$$

Finally, the analytic expression of the localization length $\xi$ can be written.

$$\frac{1}{\xi} = 2k(kg_0)^{\frac{1}{3}} F\left(\frac{sin^2\theta_{in} - \frac{\epsilon_{eff}}{\epsilon_{clad}}}{(kg_0)^{\frac{2}{3}}}\right) \tag{3.9}$$

The localization length $\xi$ and the ensemble-averaged transmission $\langle lnT \rangle$ of various $\tau_{target}$ values of realizations ($\tau_{target} = 0.5, 0.1, 0.02, 0.01$, and $\tau = 1$, periodic multilayer film or EMT homogeneous film) are plotted as a function of the incident angle $\theta_{in}$ (Fig. 3.1 and Fig. 3.2). The conventional abrupt transition of localization length $\xi(\theta)$ and average transmission across the $\theta_c$ of the homogeneous film (thick solid black line) is clear, as the wave transmission through the film across $\theta_c$ changes from Fabry–Pérot resonance to total internal reflection and the accompanying evanescent decay. In contrast, when disorder increases ($\tau_{target}$ changes from 1 to 0), the transition of the localization length

$\xi(\theta)$ (Fig. 3.1) and average transmission $\langle lnT(\theta)\rangle$ (Fig. 3.2) across $\theta_c$ tend to depart from those of the EMT case. The transition across $\theta_c$ becomes smoother due to the disorder-induced high-Q localization and higher transmission in the $\theta_{in} > \theta_c$ regime (see Fig. 3.3). It is noted that the analytically obtained $\xi(\theta)$ and $\langle lnT(\theta)\rangle$ from Eq. 3.9 (square markers) present good agreement with the numerically obtained results, with the fitting parameter of the disorder strength $g_0$ ($0.029\ nm$ for $\tau = 0.5$, $0.035\ nm$ for $\tau = 0.1$, $0.102\ nm$ for $\tau = 0.02$, and $0.213\ nm$ for $\tau = 0.01$). For even lower $\tau_{target} < 0.01$, abnormal transmission at even larger $\theta_{in}$ is possible.

The result in Fig. 3.1 and Fig. 3.2 thus reveals the correlations between the degree of disorder and the abnormal transmission, as well as the characteristic length. Most importantly, this result also demonstrates the localization control across $\theta_c$ based on the target order metric $\tau_{target}$. Considering that the disorder-induced abnormal transmission has narrowband peaks above $\theta_c$ (see Fig. 3.3), a proper choice of $\tau_{target}$ realization can be used to derive unique optical applications such as a sensitive angular filter.

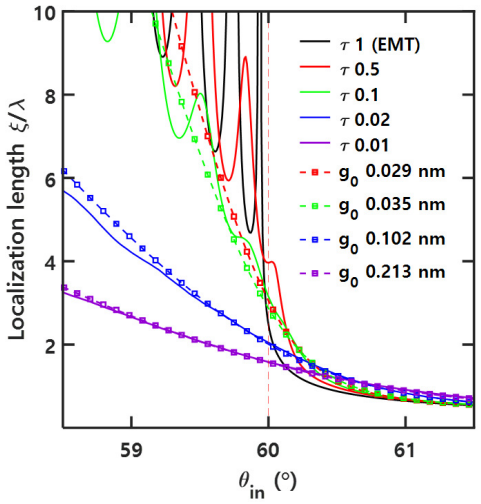


Figure 3.1: The localization length for the $\tau_{target}$ DSD film ensembles. The localization length $\xi$ is calculated from the transmission obtained with TMM. The thick solid black line indicates the localization length of the bulk EMT film. The localization length is in units of $\lambda$, the wavelength in the surrounding medium.

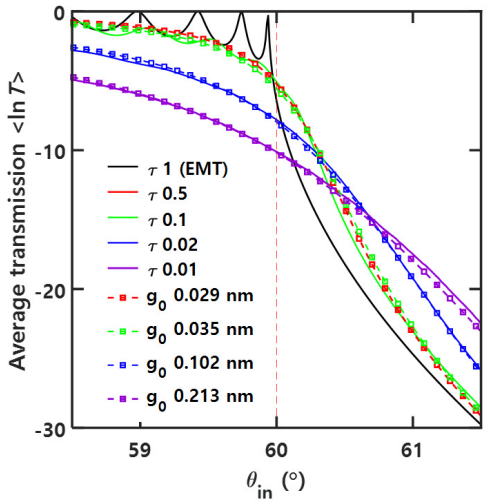


Figure 3.2: The average transmission for the $\tau_{target}$ DSD film ensembles. The colored lines are the ensemble-averaged transmission $\langle lnT \rangle$, and the square markers represent the analytically obtained localization length with fitting parameter $g_0$ from $0.03$ to $0.2$ $nm$.

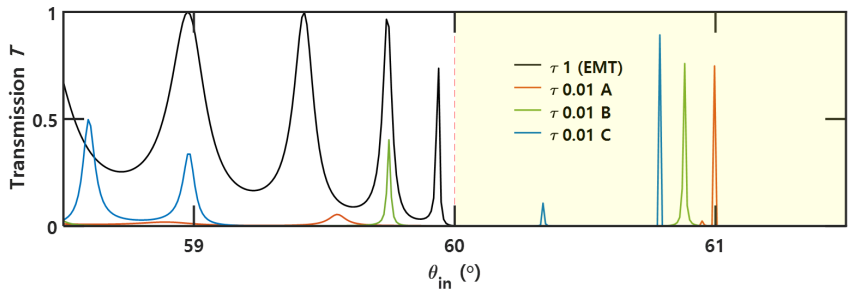


Figure 3.3: The examples of the abnormal optical responses around the critical angle, $\theta_c$. Three disordered realizations, with $\tau_{target} = 0.01$, exhibit abnormal transmission peaks above $\theta_c$.

## 3.2 Disorder scale dependency

Revealing the effect of the order metric $\tau$ on the optical properties around $\theta_c$, I further examine the effect of the scale of disorder to determine whether it is desirable to increase the number of disordered deep-subwavelength layers at the same multilayer film thickness. For this, I start from the films used in the previous section and then generate a new set of films composed of disordered layers of average permittivity within the effective layer thickness $\Lambda$. In Fig. 3.4, I plot the average transmission $\langle lnT(\theta) \rangle$ across $\theta_c$ for the new sets of films; the realizations originally have $\tau = 0.5$ and $0.01$, with $\Lambda = 40nm$ to $1000\ nm$. As $\Lambda$ increases, the average transmission $\langle lnT(\theta) \rangle$ approaches that of the EMT

result, as expected. Most interestingly, the deviation from the EMT scenario, or the emergence of abnormal transmission, is more pronounced for the films derived from highly disordered films ($\tau = 0.01$) and for smaller $\Lambda$. This result implies and confirms the role and the need for DSD structures to achieve abnormal optical properties around $\theta_c$.

## 3.3 Auxiliary Goos–Hänchen shift

Considering the above result, DSD modulates localization within the film; its effect on the GHS around the critical angle is worth investigating. The GHS is a lateral displacement of the reflected finite-cross-section beam relative to the ideal plane wave reflection at the point of incidence. In Fig. 3.5, the amount of shift on the surface $D_1$ and the corresponding parallel movement of the beam $D_2$ caused by the wave nature of the field and the propagation of the evanescent field are depicted ($D_2 = D_1 cos\theta_{in}$). This section deals with the lateral shift on the surface $D_1$ as the GHS. The GHS has been mainly discussed in the total internal reflection condition $\theta_{in} > \theta_c$, focusing on its shift length or frequency tunability. Unlike the conventional perspective of GHS tuning, where only resonance control is used [25][26][27][28], the DSD multilayer film in this paper can be considered as a generalized defect system that could provide an addi-

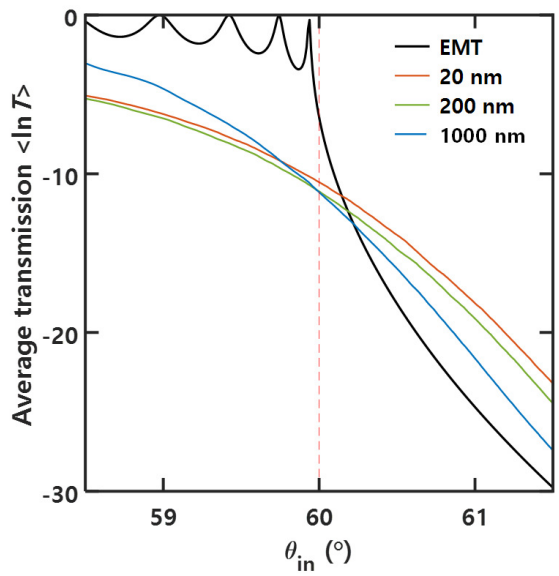


Figure 3.4: Calculated average transmission $\langle lnT(\theta)\rangle$ with various effective layer thicknesses, $\Lambda$. The new sets of films, generated using the average permittivity with $\Lambda$, are used for the calculation. The original set of realizations has $\tau = 0.01$. The colored lines represent the average transmission of $\Lambda = 20\ nm, 200\ nm$, and $1000\ nm$. The disorder-induced abnormal transmission across $\theta_c$ varies in response to $\Lambda$. $\langle lnT(\theta)\rangle$ approaches EMT (thick solid black line) as $\Lambda$ increases. For smaller $\Lambda$, the emergence of abnormal transmission (deviation from the EMT) is more pronounced, implying the role of DSD structures in inducing abnormal optical properties around $\theta_c$.

tional platform for GHS engineering. To quantitatively study the correlation between the GHS and disorder metric $\tau$, I introduce the metric of the GHS, $D_s$, which is calculated by using the phase of the reflection coefficient; first derived by Artmann using the stationary phase method [35],

$$D_s = -\frac{\lambda}{2\pi}\frac{d\phi(\theta_{in})}{d\theta_{in}} \tag{3.10}$$

where $\phi(\theta_{in})$ is the phase of the reflection coefficient at $\theta_{in}$. The calculated wavelength-normalized average GHS, $\langle D_s \rangle$, is plotted for various $\tau$ values in Fig. 3.6, taking the average from each group of $\tau_{target}$ realizations. The obtained $\langle D_s \rangle$ ranges from $0 \sim 10\ \mu m$ ($0 \sim 20\ \lambda$) at $\theta_{in} \sim 61^\circ$ ($> \theta_c$), as the wavelength in the cladding medium is $500\ nm$. It is noted that near or below $\theta_c$, $\langle D_s \rangle$ gets large for larger $\tau$. However, above $\theta_c$, where the disorder-induced abnormal transmission prevails, $\langle D_s \rangle$ dramatically increases for lower $\tau$, i.e., for highly disordered realizations. This result demonstrates that the localization induced by DSD can be used for GHS engineering by tailoring $\tau_{target}$, in addition to the existing conventional resonance control methods [25][26][27][28].

### 3.3.1 Emergence of auxiliary Goos–Hänchen shift

To provide better insight into the effect of DSD on the GHS, I use the finite element method (COMSOL Multiphysics) to determine the intensity of the electric field reflected from multilayer films with different DSD landscapes. An incident beam at $60.16^{\circ}$, above $\theta_c$, with a spatial Gaussian profile width of $4\ \lambda$ is considered using plane wave expansion. The periodic multilayer film of $\tau = 1$ and the DSD multilayer film of $\tau = 0.01$ ($A$ in Fig. 3.3) are compared. For both cases, the confinement of the field at the film boundary and the conventional GHS are observed (blue arrows in Fig. 3.7(a) and Fig. 3.7(b)) to have a lateral shift of $7.6\ \lambda$, which is in good agreement with Fig. 3.6. I note that both films exhibiting the same magnitude of GHS at different $\tau$ values implies the signature of EMT approximation on the wavelength scale. However, in contrast to Fig. 3.7(a), an auxiliary GHS is observed for the highly disordered film (Fig. 3.7(b)). With the strong localization within the DSD structure, the trapped field propagates along the x-direction and creates an auxiliary GHS of $86.4\ \lambda$, coupling with the cladding material (red arrow in Fig. 3.7(b)). The intensity of the auxiliary GHS in Fig. 3.7(b) is $\sim 1/100$ of the conventional GHS. Although the efficiency of the auxiliary GHS low, the emergence of the abnormal phenomenon and its correlation to the disorder of the system is focused on in this study.

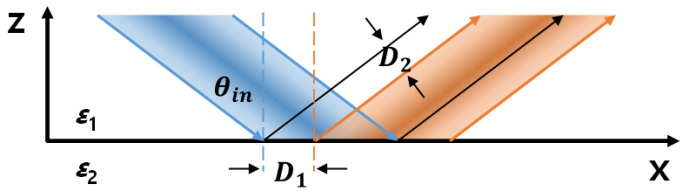


Figure 3.5: The incident beam (blue beam) and reflected beam (red beam) with a finite cross-section are the interfaces between two media with permittivity $\epsilon_1$ and $\epsilon_2$, respectively. The lateral movement along the surface ($D_1$) and the lateral movement of the beam ($D_2$) are shown.

The auxiliary GHS in a disordered structure is also observable in transverse magnetic (TM) polarized incident waves. The calculated $\langle D_s \rangle$ in TM polarization is plotted for various $\tau$ values in Fig. 3.8, taking the average from each group of $\tau_{target}$ realizations. In Fig. 3.9(a) and Fig. 3.9(b), the intensity of the magnetic field of the incidence at $40.68°$ (above $\theta_{c-TM}$, where $\theta_{c-TM} = sin^{-1}((\epsilon_{eff-TM}/\epsilon_{clad})^{\frac{1}{2}})$ and $\epsilon_{eff-TM} = \frac{2\epsilon_L\epsilon_H}{(\epsilon_L+\epsilon_H)} = 1.67$) with a spatial Gaussian profile width of $4\ \lambda$ is depicted. The disordered film used in Fig. 3.9(b) is the same realization as that in Fig. 3.7(b). As in Fig. 3.7(a) and Fig. 3.7(b), both cases have the conventional GHS of $5.3\ \lambda$ (blue arrows in Fig. 3.9(a) and 3.9(b)), which is in good agreement with Fig. 3.8, while an auxil-

iary GHS of $83.9\ \lambda$ is also observable in the disordered case (red arrow in Fig. 3.9(b)).

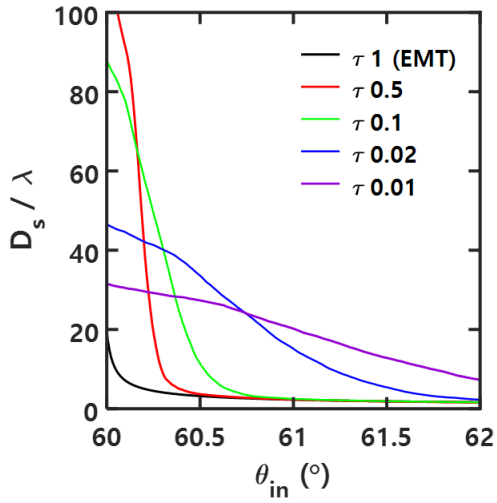


Figure 3.6: The ensemble-averaged GHS for each group of $\tau_{target}$ realizations (TE polarization). The GHS calculation is based on Eq. 3.9. Above $\theta_c$, the GHS becomes larger at low $\tau$ realizations.

### 3.3.2 Disorder-induced localization hubs

Since the auxiliary GHS is caused by disorder and the trapped field within the film is visible in Section 3.3.1, the abnormal field profile should be explained in a simple manner. In Fig. 3.7(b) and Fig. 3.9(b), there are the overlapping yellow lines that depict the effective permittivity variations through the thick-

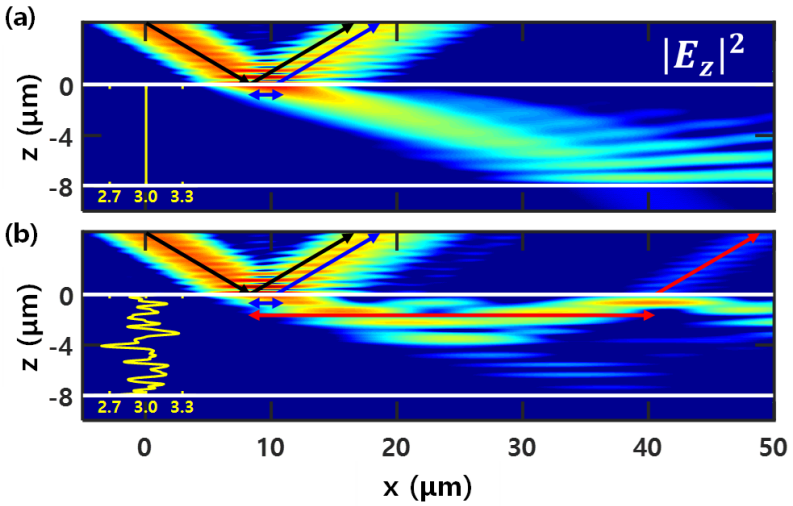


Figure 3.7: The calculated electric field distribution in the (a) periodic and (b) disordered ($A$ in Fig. 3.3) films. The conventional GHS (blue arrow) is observed in both cases. In (b), the trapped field and an auxiliary lateral shift (red arrow) are depicted. The emergence of the auxiliary shift originates from the localized field, which is trapped and propagated along the positive x-direction and results in an 11-fold enhancement from the conventional shift. The total thicknesses $L$ of the films are the same, $8\ \mu m$.

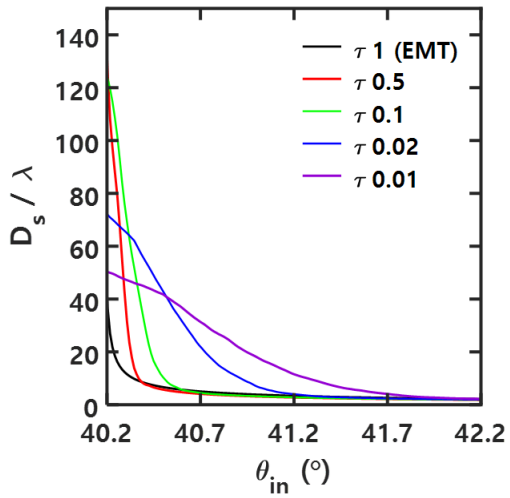


Figure 3.8: The ensemble-averaged GHS for each group of $\tau_{target}$ realizations (TM polarization).The GHS calculation is based on Eq. 3.9. Above $\theta_c$, the GHS becomes larger at low $\tau$ realizations.

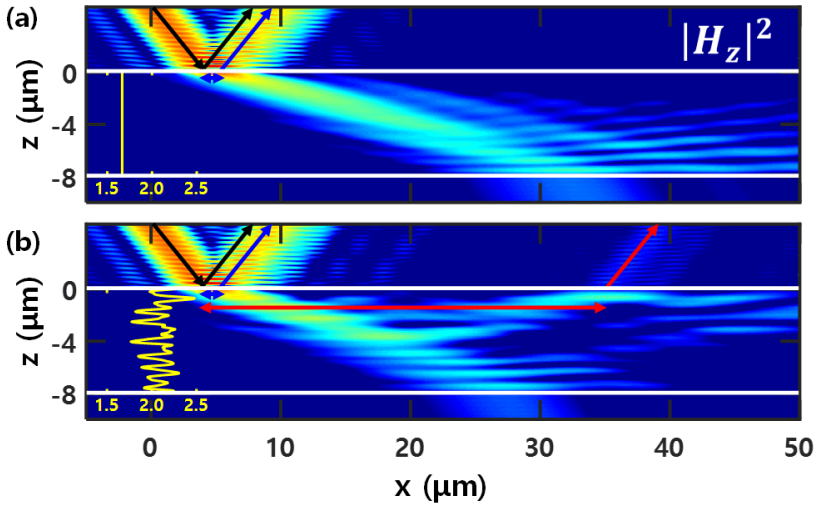


Figure 3.9: The calculated magnetic field distribution of the TM polarized incidence on (a) periodic and (b) disordered ($A$ in Fig. 3.3) films. The conventional GHS (blue arrow) is observed in both cases. In (b), the trapped field and an auxiliary lateral shift (red arrow) are depicted. As in TE polarization, the emergence of the auxiliary shift originates from the localized field and results in a 15-fold enhancement from the conventional shift. The total thicknesses $L$ of the films are the same, $8\ \mu m$.

ness domain $z$ on the wavelength scale. The detailed calculation of the effective permittivity calculation is demonstrated in Fig. A.1. Here, the average window of $1\ \lambda$ is used from now on.

Fig. 3.10 shows the matching between the localized field intensity and the effective permittivity fluctuation along with the $z$ domain. As the localized field locations within the film match the high permittivity peaks, thus it is proved that the auxiliary GHS beam in the DSD film has an additional degree of freedom for GHS engineering utilizing disorder, unlike conventional GHS tuning based on surface resonance control. The localized positions within the film are now named "localization hubs".

### 3.3.3 Disorder-induced localization control

Previously, the importance of the localization hubs in creating the abnormal wave propagation within the film is emphasized. Thus, controlling the localization hubs will lead to the tuning of the auxiliary GHS. The question is how sensitively the localization hubs will respond to the mere perturbation. In Fig. 3.11, the auxiliary GHS control using only a single-layer thickness variation in a deep-subwavelength scale ($0.005\ \lambda$) is shown. The single-layer thickness fluctuation changes the effective permittivity profile, Fig. 3.11(a), and causes the wavelength scale lateral shift variation ($2\ \lambda$) in Fig. 3.11(b). Considering

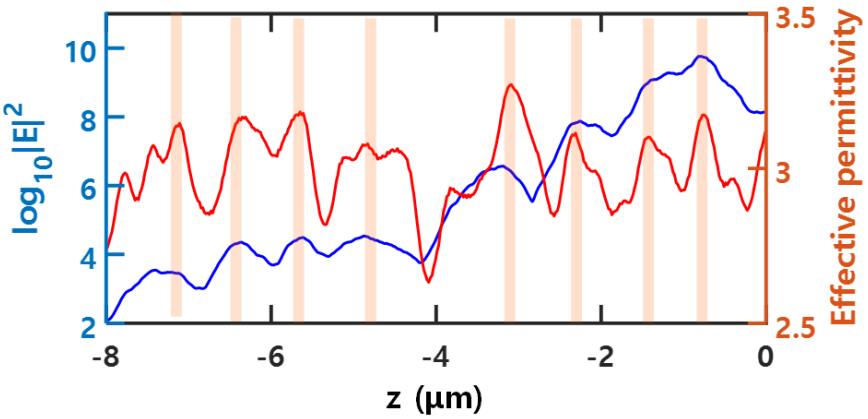


Figure 3.10: The overlapping lines depict the effective permittivity variations through the thickness domain $z$ on the wavelength scale (Red) and the averaged electric field intensity within the disordered film over $x$ domain (Blue). The localized field locations within the film match the high permittivity peaks.

the thickness fluctuation is ignorable in the view of EMT and the order metric $\tau$, the result provides the auxiliary GHS is tunable using the localization hubs "within" the film, and the localization hubs are extremely sensitive. It should be noted that not all localization hubs are effective. One or a few major hubs exist that are the most effective for the wave propagation path and are defined as the main localization hubs. In Section A.3, the single-layer thickness variation is applied to nearby peaks and dips of the effective permittivity profile and verified the concept of the main localization hub shown in Fig. A.2 is valid.

## 3.4 Conclusion

In this chapter, I demonstrate the abnormal optical responses of the localization length and the transmission above $\theta_c$. The abnormal transmission peaks caused by the disorder-induced strong localization result in the smooth transition at $\theta_c$. The conditions for abnormal transmission peaks are strongly correlated with the disorder strength. Thus, the smoother transition for low $\tau$ films is observed.

I also introduce the auxiliary GHS, which is different in the fundamental principle compared to the conventional GHS. The incident wave at $\theta_c$ evanescently transmits through the disordered film. It interacts with the localization hubs, creating the lateral propagation of the trapped field and leaking out to the

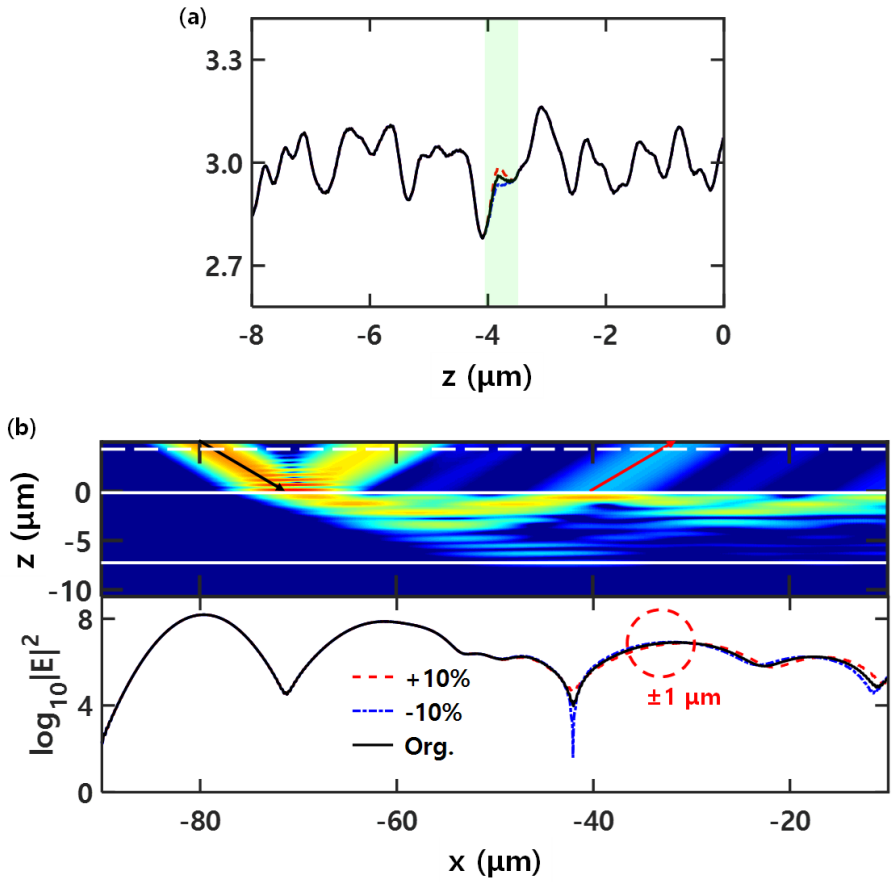


Figure 3.11: (a) The variation of the effective permittivity profile with only a single-layer thickness variation in a deep-subwavelength scale ($0.005\ \lambda$) (b) The calculated electric field distribution of the TE polarized incidence of the original disordered film (Top) The field intensity variation on the dotted line (Bottom) depicts the wavelength scale lateral shift variation ($2\ \lambda$) due to $\pm 10\%$ perturbation of the single-layer thickness variation.

reflecting side, which has an 11-fold enhancement from the conventional shift. The existence and the importance of the localization hubs are defined, and the correlation with the thickness disorder of the film is studied.

The concept of the localization hubs is similar to the subregion defined by the localization landscape in [36]. In [36], the subregions are surrounded by the connecting landscape valley. It is confirmed that the localization is limited to a single subregion or neighboring subregions in the case of a high-energy mode. Both methods have an advantage in that the localization boundaries can be pre-defined only with structural features. The localization hub analysis has the advantage of identifying the main localization hub.

Finally, the control of the correlated lateral shift length of the auxiliary GHS with the perturbation of the localization hubs is achieved using deep-subwavelength disorder in a single-layer thickness.

# Chapter 4

# SYMMETRIC DISORDER DESIGN

This chapter proposes the symmetric design method of disordered media, which is not limited to optical domain but including general wave systems. The abnormal phenomena of shifted transmission is discussed in the manner of the localization hubs as well.

## 4.1 Symmetry on disorder

As concluded in Section 3.4, the auxiliary GHS in the disordered film is closely related to the wave propagation through the localization hubs. In the case of the auxiliary GHS, the trapped field propagates in the lateral direction and reflects back to the reflecting side of the film. The localized field only reflects back to the reflecting side because the leakage path caused by the interaction between

the localization hubs is only valid to the reflecting direction.

Therefore, in order to realize a lateral shift on the transmitting side, symmetry to the disordered multilayer film is applied. Placing the mirrored set of disorder from the reflecting side to the localization hub toward the transmitting side would create a leakage path. The transmission through the path will be via the localization hubs, which are controllable using disorder engineering.

## 4.2 Symmetry-induced transmission shift

The definition of the symmetric disorder in the following is a mirrored placing of the disorder that controls the localization hubs and creates a propagation path of the localized field toward the transmission side. Fig. 4.1(b) details the electric field intensity in such a symmetry-fold disordered film, where thickness distribution is symmetrical in the middle of the film. Fig. 4.1(b) shows two types of transmission; enhanced transmission (blue arrow) compared to that of Fig. 4.1(a) and the emergence of auxiliary transmission (red arrow) through the propagation via mirror-folded localization hubs. It is noted that the laterally-shifted transmission only exists in Fig. 4.1(b) (red arrow), and an additional translational shift of $80\ \lambda$ compared to the auxiliary GHS in Fig. 4.1(a) is evident.

The difference between Fig. 4.1(a) and Fig. 4.1(b) can be explained by the differences in their profile of effective permittivity fluctuation (Fig. 4.2(a) and Fig. 4.2(b)). In the original disordered film (Fig. 4.1(a)), there exists a high permittivity optical potential gap (strong localization hub) between $-3$ to $-4$ $\mu m$ in the film depth direction. When the evanescent tunneling wave experiences such a large gap, the possibility of tunneling diminishes, resulting in strong localization. In contrast, for the symmetric disordered film (Fig. 4.1(b)), the regularly distributed localization hubs balance the wave localization and tunneling.

## 4.3 Conclusion

In this chapter, I suggest the symmetric disorder to create the wave propagation path through the localization hubs for the shifted transmission. The main idea is to provide the leakage path for the trapped field, which is realized in the mirrored placing of the disorder. As a result, $80$ $\lambda$ of enhancement in the lateral shift of transmission compared to the auxiliary GHS in the engineered disorder film.

The difference in the avarage permittivity profile provides a better understanding of the phenomenon and opens the possibility of the inverse design

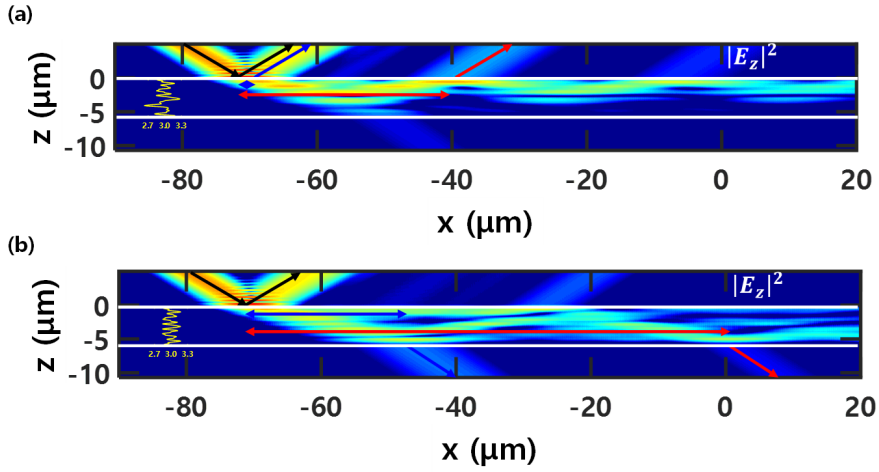


Figure 4.1: The calculated electric field distribution (TE polarization) of the engineered disorder film and the symmetric disorder film. In (a), the trapped field and an auxiliary lateral shift (red arrow) in the engineered disorder film are depicted. The emergence of the auxiliary shift originates from the localized field, which is trapped and propagated along the positive $x$-direction and results in an $11$-fold enhancement from the conventional shift. In (b), the extended path of the propagating field and the enhanced transmission shift (red arrow) in the symmetric disorder film are depicted. The lateral transmission shift comes from the balance between wave localization and tunneling and is $80\ \lambda$ longer than the auxiliary GHS in (a).

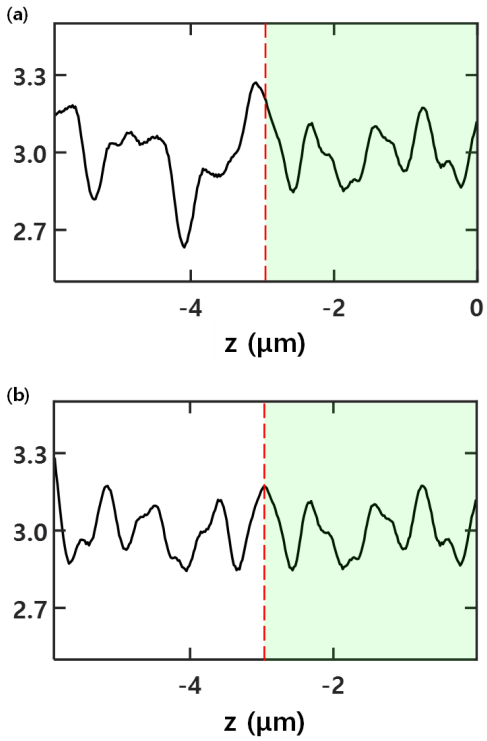


Figure 4.2: The effective permittivity profile of the engineered disorder film and the symmetric disorder film. (a) and (b) are the effective permittivity profile of Fig. 4.1(a) and 4.1(b), respectively. The thickness and EMT of both films are the same.

with the designed permittivity profile. Our proposal and result reveal a new and interesting phenomenon of transmission shift in a thin multilayer film through the application of symmetry toward disorder-induced localization.

# Chapter 5

# CONCLUSION

This dissertation demonstrates the $\tau$-oriented disorder engineering in the planar multilayer films, followed by the abnormal optical responses of the localization length, transmission, and the auxiliary GHS, which are induced by deep-subwavelength disorder. By applying the order metric $\tau$ as a target to the inverse engineering of disorder, the iterative disorder engineering has generated normally distributed disorder films with the thickness variation in units of $\lambda/5,000$. It is worth to note that a similar approach with different material phase spaces would also be possible by modifying and engineering the probability density function in the perturbation. The disorder-induced localization causes the abnormal transmission and the smooth localization length transition around the critical angle. The result is in excellent agreement with the theoretical analysis developed for randomly stratified dielectric media. Considering

that the disorder-induced abnormal transmission has narrowband peaks above $\theta_c$, the localization control using the order metric-based disorder engineering shows potential for unique optical applications, such as a sensitive angular filter. I also emphasize the emergence of the auxiliary GHS, as its fundamental principle is different from the conventional GHS. I define the localization hubs and clarify their importance and role in understanding the abnormal phenomenon. It is concluded that the incident wave at $\theta_c$ evanescently transmits through the disordered film and interacts with the localization hubs. This creates the lateral propagation of the trapped field and leaks out to the reflecting side. In the demonstrated realization of the disordered film, the auxiliary GHS achieves an 11-fold enhancement from the conventional GHS. Demonstrating the auxiliary GHS tuning using deep-subwavelength disorder in a single-layer thickness provides promising applications in the engineered disorder based on localization hubs. Finally, the laterally shifted wave transmission is found for the first time by applying symmetry to disorder. The main idea is to provide the wave propagation path for the trapped field, which is realized in the mirror-folding of the disorder. The adoption of symmetry balances the wave localization and tunneling through the localization hubs. It results in the $80\ \lambda$ enhanced transmission shift compared to the auxiliary GHS in the engineered disorder film. The newly suggested disorder symmetry and the transmission shift in a

multilayer film allow designing localization hub distribution and open the potential application in angular filtering and sensing, not limited to the optical domain but including general wave systems.

Demonstrating valid disorder engineering schemes and wave phenomena interact with disorder, this work would achieve the full potential of the disordered media in designing the abnormal optical responses and their applications and will expand the range of disorder application to the conventional photonics.

# Chapter A

# Supplements for Chapter 3

## A.1 Effective permittivity profile

The effective permittivity profile defined in Section 3.3.2 represents the disordered film seen on the wavelength scale. As the layer thicknesses of the disordered films and their variations in this dissertation are deep-subwavelength scales, the effect of each layer should be ignorable. However, they can affect their surroundings and intervene in the wave-disorder interaction as an indirect effect.

To represent this indirect effect, I used Gaussian summation over the average window of the wavelength scale. The window is different from the effective layer thickness, $\Lambda$, in Section 3.2, where the former is weighted in Gaussian profile, and the latter is a simple average.

Fig. A.1 shows the variation of the permittivity profile over the film. Here, the film is $A$ in Fig. 3.3 and the permittivity profiles for different average windows are depicted. As the average window increases from the original profile (black line in Fig. A.1) to $1\ \lambda$ average (red line in Fig. A.1), the fluctuation smoothens, and the locations of high permittivity groups become clear. The average window is five times the standard deviation of the Gaussian weight profile.

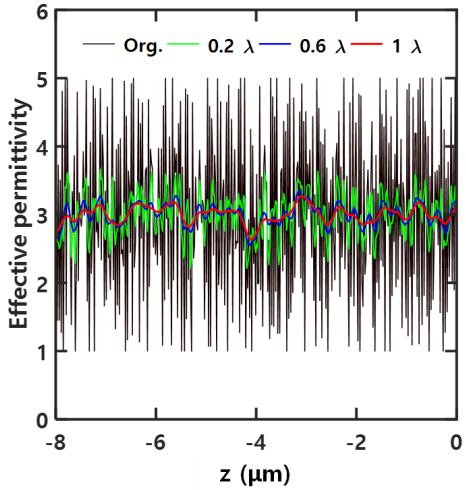


Figure A.1: The overlapping lines depict the effective permittivity variations through the thickness domain $z$ on different average windows. The black line is the original variation, green for the average window of $0.2\ \lambda$, blue for $0.6\ \lambda$, and red for $1\ \lambda$.

## A.2 Localization hubs in disorder systems

In Section 3.3.2, I defined the localization hubs for only one realization, but generalization is needed for universal adoption of the concept and pioneering field of application. Fig. A.2 shows the correspondence between the localized field intensity and the effective permittivity fluctuation along with the $z$ domain in $A$, $B$, and $C$ in Fig. 3.3. It can be seen that the effective permittivity profile and the localization hubs are substantially consistent in all three realizations.

The variation in the effective permittivity profile can also be referred to as the fluctuation in optical potential, and not all potential peaks are indeed localization hubs. Considering the tunneling probability of the propagating wave passing through the optical potential, the locations of extreme potential differences, as in $-4\ \mu m$ in Fig. A.2(a), $-2\ \mu m$ in Fig. A.2(b), and $-1\ \mu m$ in Fig. A.2(c), are considered the most important localization hubs (red arrows in Fig. A.2 and Fig. A.3. The localization hub analysis based on the optical potential is proven effective in Fig. A.3, demonstrating the field intensity within the films and their auxiliary GHS.

As the leakage wave propagation to the reflecting side is caused by multiple interactions with the disordered system, the multiple auxiliary GHS can be observed with the numerous wave propagation paths (Fig. A.3(b)). In Fig.

A.3(c), the auxiliary GHS is not visible, unlike Fig. A.3(a) and Fig. A.3(b). The main localization point is located too close to the reflecting side of the film, at $-1\ \mu m$, resulting the minor effect of the disorder-induced localization.

## A.3 Localization hub control

The control of the auxiliary GHS using a single-layer thickness modification that the variation is in deep-subwavelength scale is discussed in Section 3.3.3. The controllability and importance of the main localization hub can be reconfirmed by confirming that the main localization hub responds sensitively without affecting the EMT and the order metric of the film.

In this section, I further look into the effect of the surrounding localization hubs in addition to the result in Section 3.3.3. Fig. A.4(a) to (d) shows the variation at the major inflection points of the effective permittivity profile using the single-layer thickness change. The corresponding effect on the auxiliary GHS is depicted in Fig. A.4(e) to (h). In Fig. A.4(a) to (d), the blue area represents the $10\%$ variation of a single-layer thickness. Fig. A.4(c) and A.4(g) is the same for Fig. 3.11(a) and Fig. 3.11(b), and the reflection intensity profile due to the variations in the peak Fig. A.4(f) and the dip Fig. A.4(h) are ignorable. As the peaks and the dips define the potential well of the main localization hub, small

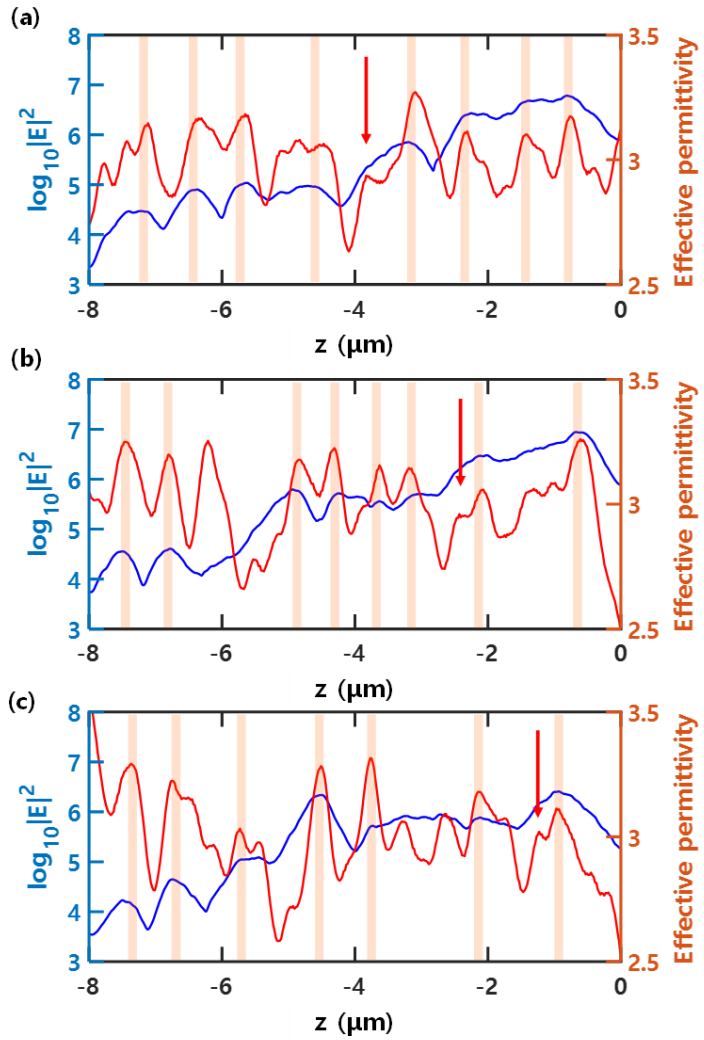


Figure A.2: The overlapping lines depict the effective permittivity variations through the thickness domain $z$ on the wavelength scale (Red) and the averaged electric field intensity within the disordered film over $x$ domain (Blue) in $A$, $B$, and $C$ in Fig. 3.3. The red arrows indicate the main localization hubs.

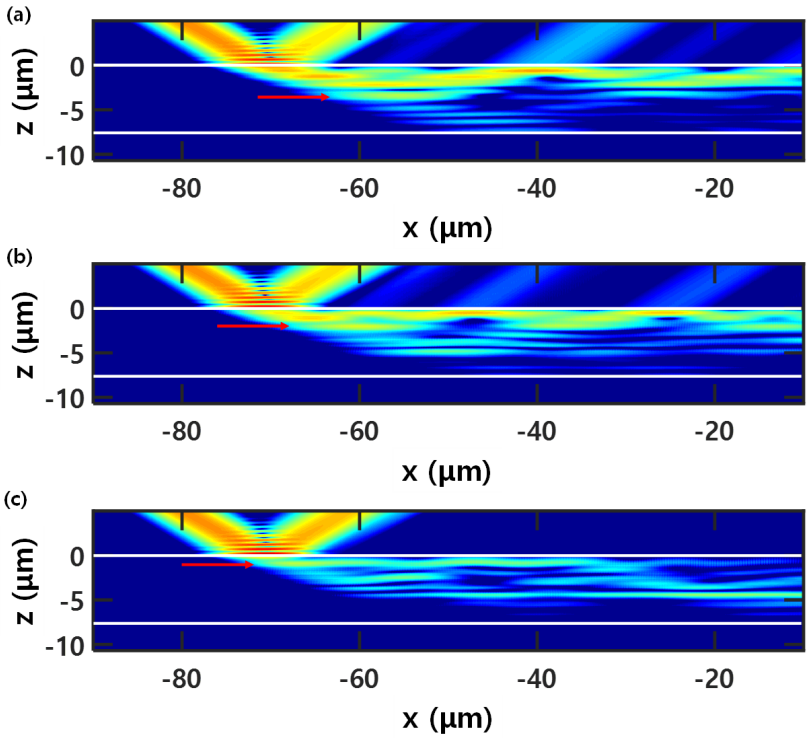


Figure A.3: The calculated electric field distribution in $A$, $B$, and $C$ in Fig. 3.3.

The red arrows indicate the main localization hubs.

variations are ineffective to the wave response. Fig. A.4(e) shows a difference in the second auxiliary GHS. Multiple reflections between localization hubs cause multiple auxiliary GHS, and the shallow localization hubs govern the follow-up auxiliary GHS.

Conclusively, although the localization hubs are sensitive, to control the auxiliary GHS, the perturbation should be applied to the main localization hub. Although the amount of change is not large compared to the enhancement of the auxiliary GHS, it is meaningful in confirming the role and importance of the main localization hub.

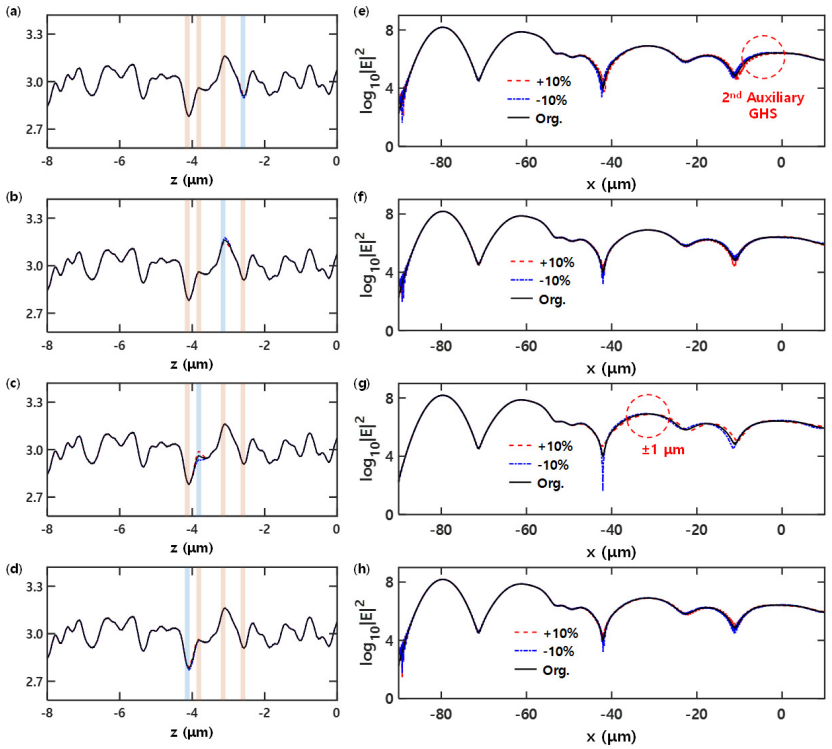


Figure A.4: The effective permittivity variations due to the single-layer thickness variation of $A$ in Fig. 3.3 in (a) to (d). The corresponding result of the calculated electric field intensity at the reflecting side of the film in (e) to (h). Black line is the original, Red dotted is $+10\%$, and Blue dotted is $-10\%$ variation of a single-layer thickness, respectively.

# Chapter B

# Supplements for Chapter 4

## B.1 Symmetric design and localization hubs

The disorder-induced transmission shift at the arbitrary angle is introduced for the first time in this dissertation. In Section 4.2, the mirrored system causes the transmission shift is suggested. In this section, the same system is folded at various positions and shows important characteristics in localization hub designing. The mirror symmetry can enhance peaks or dips in the view of the effective permittivity profile. Following case studies provide insight into the wave-disorder interaction in the permittivity profile perspective and the design ideas for desired wave phenomena.

Fig. B.1 and Fig. B.3 show the effect of symmetry on the permittivity profile. The black lines are the original permittivity profile of $A$ in Fig. 3.3, and

the red lines are the permittivity profile of the mirrored films folded at various layers. In the discussion of the localization hubs, the permittivity peaks are in good correlation to the trapped field intensity (Section 3.3.2).

As the basic idea of the transmission shift is to guide the trapped field to leak toward the transmitting side, the peak modulations are the first to discuss. Fig. B.1 and Fig. B.2 depict the effective permittivity profiles at the symmetric films and the corresponding electric field intensity calculation, respectively. Fig. B.2(a) and (b) display different amount of the transmission shift. Other than the auxiliary GHS, transmission and the auxiliary GHS positions are the same. Between Fig. B.1(a) and Fig. B.1(b), the folded layers locate within the localization hub and between the hubs. As the peak in Fig. B.1(a) at $-2.5\mu m$ enhances, the localized field intensity at $-2\mu m$ increases, accelerating the auxiliary GHS with a smaller lateral shift. In Fig. B.2(a), it can be seen that the transmission shift appears relatively short as the lateral propagation of the localized field decreases. On the other hand, in Fig. B.1(b), the main localization hub works properly because the back and forth of the folded location has a similar peak size and thus creates the balance between tunneling and localization of the field. Additionally, lateral propagation of the tunneling wave follows the shifted transmission path as intended (Fig. B.2(b)). The importance of the folded layer position can be seen from Fig. B.2(a) and Fig. B.2(b). The change

from Fig. B.2(b) to Fig. B.2(e) is about the effect of the peak size of the permittivity profile. The increased peak blocks the tunneling field in Fig. B.2(d) and Fig. B.2(e), where the shifted transmission disappears and the multiple auxiliary GHS due to the reflection at the folded layer can be seen.

Secondly, the modulations on dips are to be discussed. Fig. B.3 and Fig. B.4 depict the effective permittivity profiles at the symmetric films and the corresponding electric field intensity calculation, respectively. The folded system in Fig. B.3(a) has an enhanced dip with the folded layer close to the previous peak modulation in Fig. B.1(a). The wave within the film of Fig. B.4(a) is rather similar to that of Fig. B.2(c), except for the shifted transmission. The laterally propagating wave is blocked as there is a large optical potential gap between the transmitting side of the film and the lowest dip at the folded layer. As in the peak enhancement, the dip strengthening is not always constructive in achieving the shifted transmission. Fig. B.3(b) to (e) show the change in wave propagation according to the dip profile variation at similar positions. Although the transmission shift appears in Fig. B.4(b) since the main localization point is located at $-2\mu m$, the lateral shift length is much shorter than Fig. B.2(c). As the dip at the folded layer increases from Fig. B.4(b) to (d), the enhanced optical potential results in the multiple auxiliary GHS as in Fig. B.2(e). When the potential wall is high enough, transmitting wave is blocked, and transmission

is not observed in Fig. B.4(c) and (d). The un-shifted transmission reappears in Fig. B.4(e) with the effect of the small peak replacing the high dip. Therefore, it can be concluded that the control of the dip height could not lead to the implementation of the transmission shift.

In this section, we looked at the increment of peaks and dips due to the folded layer location of the mirror symmetry film. In summary, the locations of peaks and dips in the permittivity profile play an important role in controlling the main localization hubs when their heights are close to or slightly larger than the nearby variations. The deeper the main localization hub is, the longer the lateral propagation and the higher the expected value of the auxiliary GHS or the transmission shift. It is possible to induce the leakage of the confined wave propagating on the lateral axis by adjusting the permittivity profile peak size. The effect is the greatest when the surrounding peak values have a gradual distribution. This dissertation opens the possibility of the designed effective permittivity profile, which has an arbitrarily adjustable auxiliary GHS or transmission shift. Further study on the inverse engineering of the deep-subwavelength film, based on the designed effective permittivity profile, is required for expanded application areas.

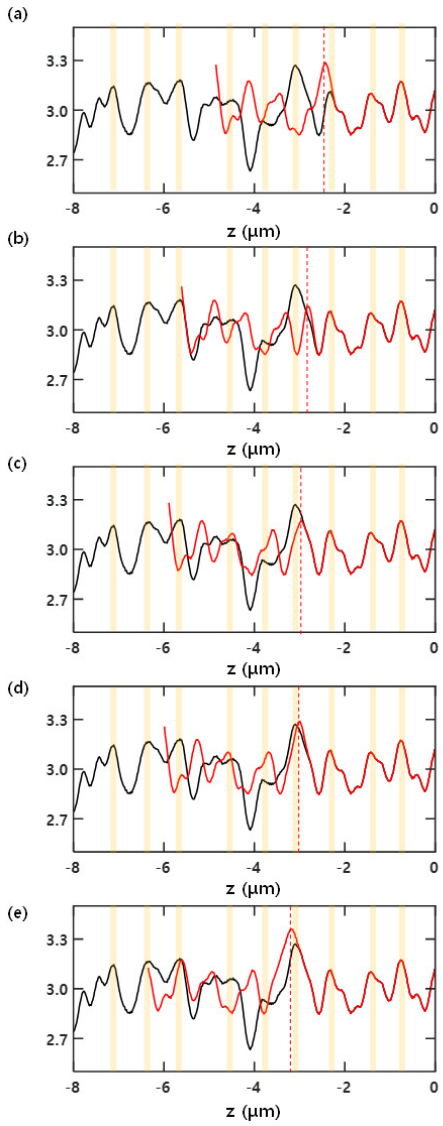


Figure B.1: The overlapping lines depict the effective permittivity profiles of the folded films (Red) and the original film (Black). The red dotted lines indicate the folded layer locations, and highlighted areas imply localization hubs.

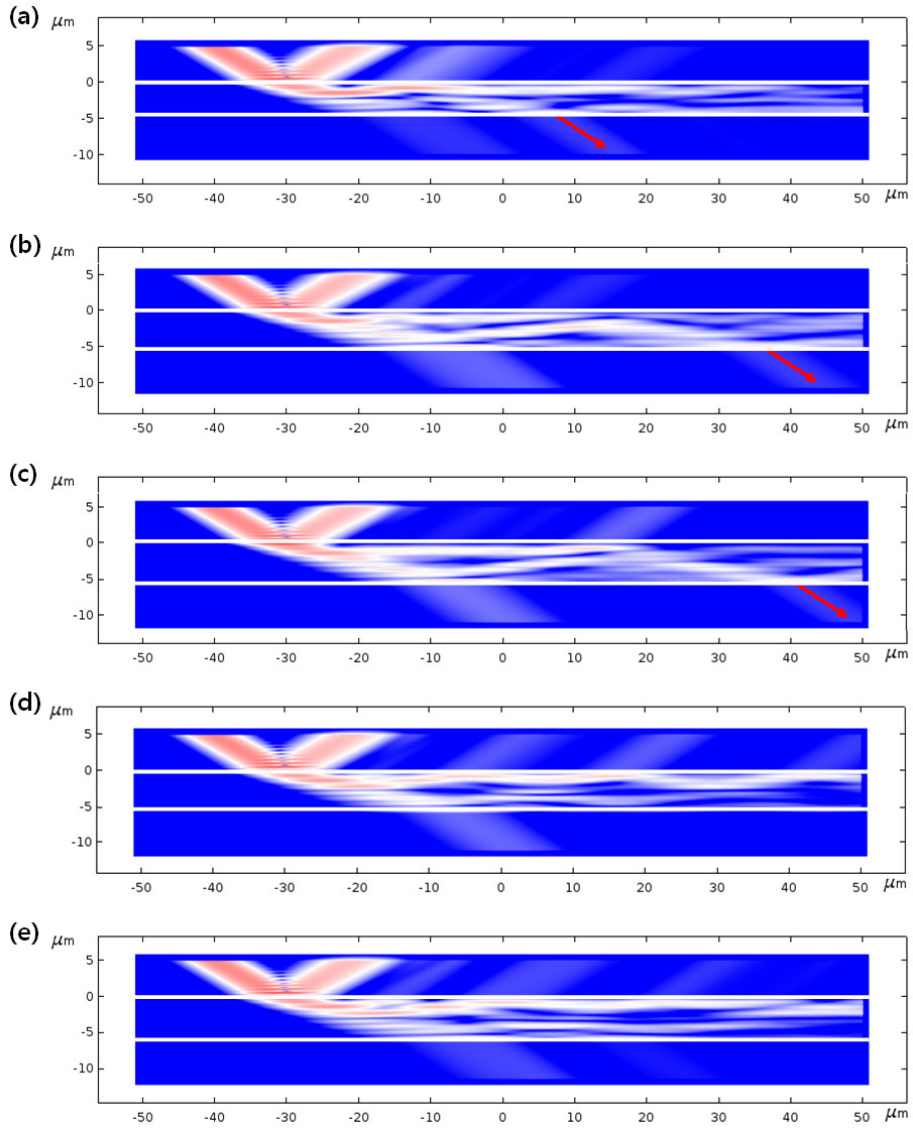


Figure B.2: The calculated electric field distribution in the symmetric disordered films. The transmission shift is visible in (a), (b), and (c), while (d) and (e) have enhanced reflection due to the increased permittivity peak.

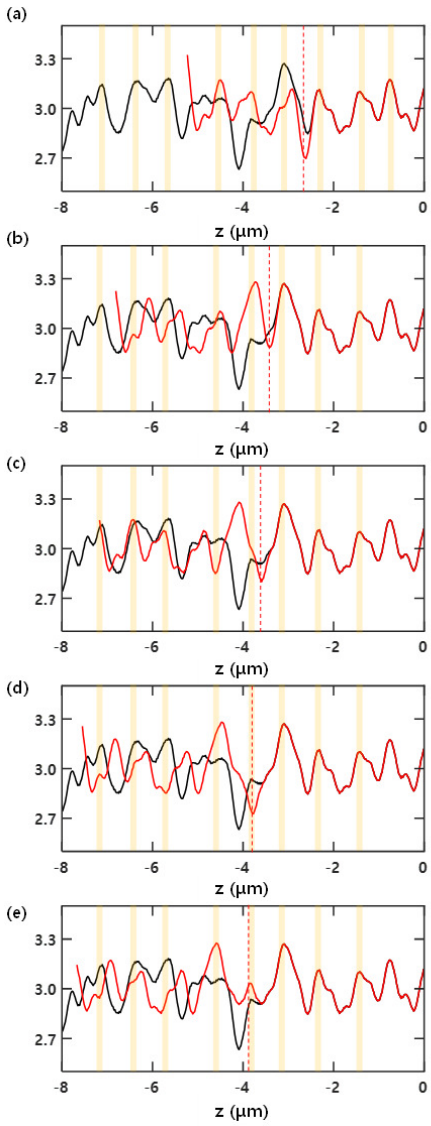


Figure B.3: The overlapping lines depict the effective permittivity profiles of the folded films (Red) and the original film (Black). The red dotted lines indicate the folded layer locations, and highlighted areas imply localization hubs.

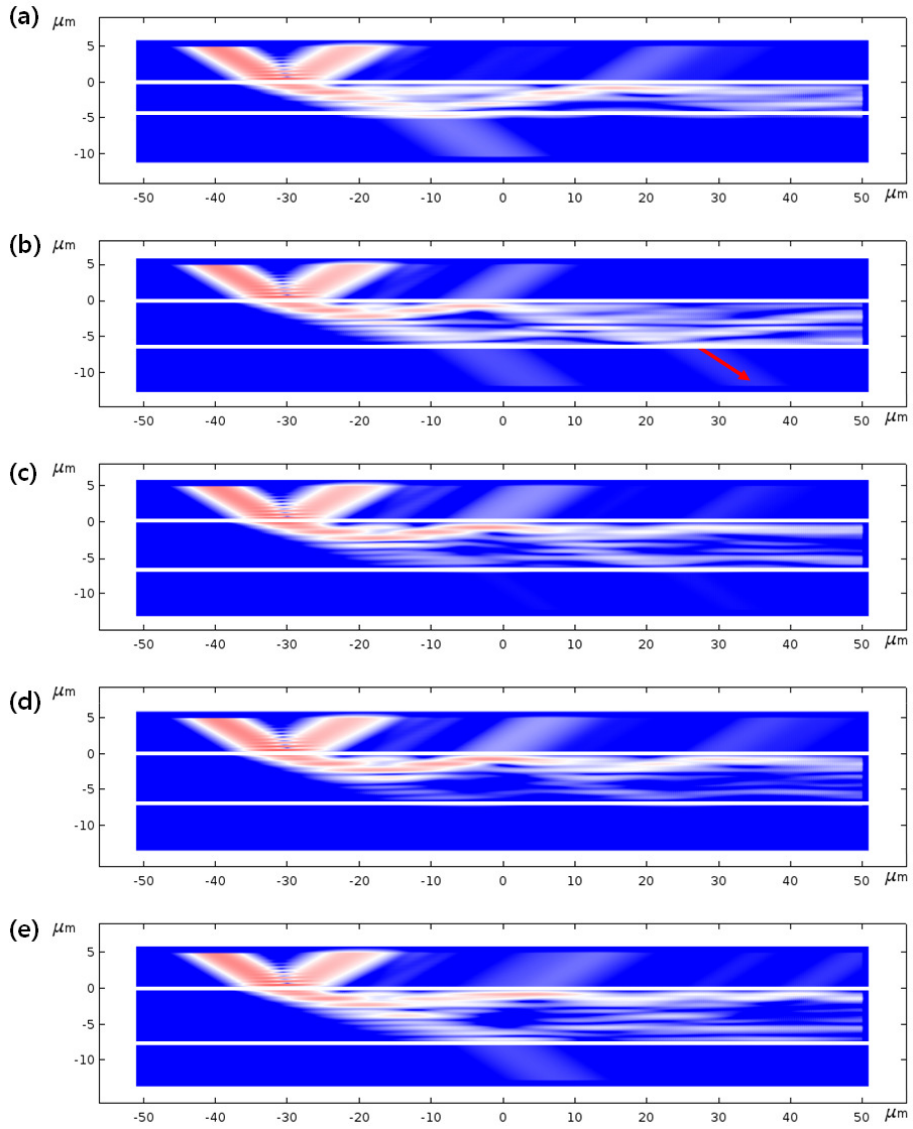


Figure B.4: The calculated electric field distribution in the symmetric disordered films. The transmission shift is visible in (b), while (c) and (d) demonstrates no transmission due to the increased permittivity dip.

## B.2 Asymmetric case study

So far, I have looked at the trends of wavelength propagation, auxiliary GHS, and transmission shift according to the effective permittivity profile variations. The mirror symmetry is only considered for transmission shifting. Still, taking the advice that transmission shifting can be implemented even if it is not perfectly symmetrical, in this section, I demonstrate the transmission shift can be generated even in an asymmetrical structure.

Fig. B.5(a) and Fig. B.5(b) show the effective permittivity profile and the field intensity response of the combined realization using different portions of $A$ in Fig. 3.3 at different $z$ domains. The non-mirror symmetric effective permittivity profile, Fig. B.5(a) right, is similar to Fig. 4.2(b) and the transmission shift is observed as well. The combination of the portions of different realizations can also achieve the transmission shift as an asymmetric design of disorder. In Fig. B.5(c) and Fig. B.5(d) show the effective permittivity profile and the field intensity response using $A$ and $B$ in Fig. 3.3. With a proper weaving of the effective permittivity profiles, the transmission shift is emerged in Fig. B.5(d).

As a result of the case study, it is found that mirror symmetry is not the only way to generate the transmission shift, and the localization hub distribution is

important, as previously discussed. Although the mirror-folding symmetry has advantages in terms of design complexity, it is meaningful that the inverse engineering scheme for the transmission shift can be extended to the asymmetric system.

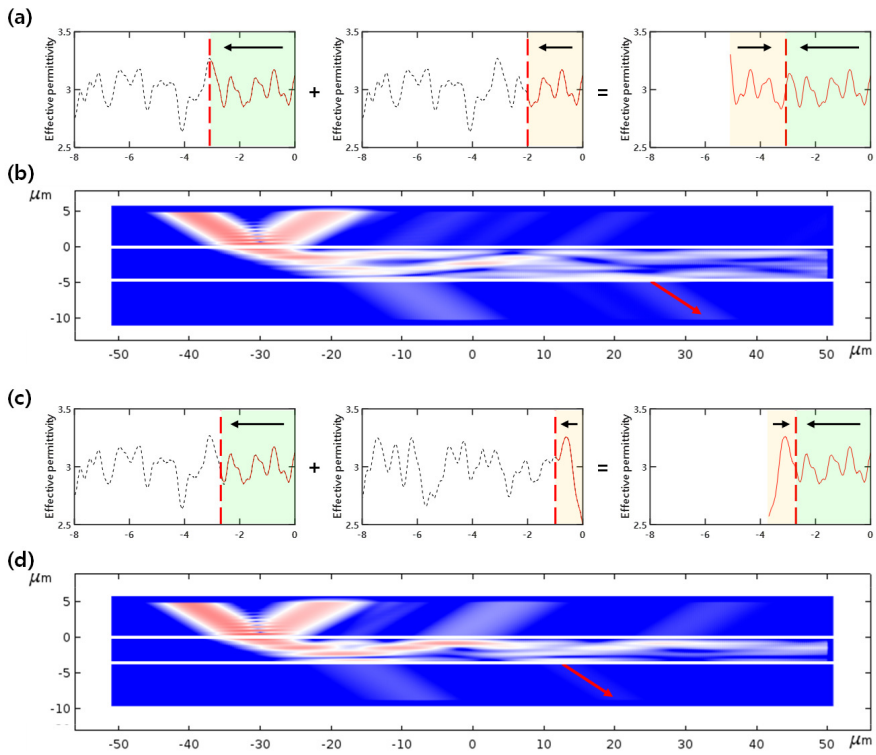


Figure B.5: The asymmetric effective permittivity profile and the calculated electric field distribution using different portions of $A$ in Fig. 3.3 ((a) and (b)). The same results using portions of different realizations of $A$ and $B$ in Fig. 3.3 ((c) and (d)). The transmission shift is achieved in asymmetric disordered systems.

# Bibliography

[1] P. W. Anderson. Absence of diffusion in certain random lattices. *Phys. Rev.*, 109:1492–1505, Mar 1958.

[2] Hanan Herzig Sheinfux, Ido Kaminer, Azriel Z. Genack, and Mordechai Segev. Interplay between evanescence and disorder in deep subwavelength photonic structures. *Nature Communications*, 7(1):12927, Oct 2016.

[3] Hanan Herzig Sheinfux, Yaakov Lumer, Guy Ankonina, Azriel Z. Genack, Guy Bartal, and Mordechai Segev. Observation of anderson localization in disordered nanophotonic structures. *Science*, 356(6341):953–956, 2017.

[4] Anatoly Patsyk, Uri Sivan, Mordechai Segev, and Miguel A. Bandres. Observation of branched flow of light. *Nature*, 583(7814):60–65, Jul 2020.

[5] Pierre Barthelemy, Jacopo Bertolotti, and Diederik S. Wiersma. A lévy flight for light. *Nature*, 453(7194):495–498, May 2008.

[6] B. L. Altshuler, D. Khmel'nitzkii, A. I. Larkin, and P. A. Lee. Magnetoresistance and hall effect in a disordered two-dimensional electron gas. *Phys. Rev. B*, 22:5142–5153, Dec 1980.

[7] Sunkyu Yu, Cheng-Wei Qiu, Yidong Chong, Salvatore Torquato, and Namkyoo Park. Engineered disorder in photonics. *Nature Reviews Materials*, 6(3):226–243, Mar 2021.

[8] Salvatore Torquato and Frank H. Stillinger. Local density fluctuations, hyperuniformity, and order metrics. *Phys. Rev. E*, 68:041113, Oct 2003.

[9] Salvatore Torquato. Hyperuniform states of matter. *Physics Reports*, 745:1–95, 2018. Hyperuniform States of Matter.

[10] Jaeuk Kim and Salvatore Torquato. Characterizing the hyperuniformity of ordered and disordered two-phase media. *Phys. Rev. E*, 103:012123, Jan 2021.

[11] D. Chen and S. Torquato. Designing disordered hyperuniform two-phase materials with novel physical properties. *Acta Materialia*, 142:152–161, 2018.

[12] Robert D. Batten, Frank H. Stillinger, and Salvatore Torquato. Classical disordered ground states: Super-ideal gases and stealth and equi-luminous materials. *Journal of Applied Physics*, 104(3):033504, 2008.

[13] Marian Florescu, Salvatore Torquato, and Paul J. Steinhardt. Designer disordered materials with large, complete photonic band gaps. *Proceedings of the National Academy of Sciences*, 106(49):20658–20663, 2009.

[14] Weining Man, Marian Florescu, Eric Paul Williamson, Yingquan He, Seyed Reza Hashemizad, Brian Y. C. Leung, Devin Robert Liner, Salvatore Torquato, Paul M. Chaikin, and Paul J. Steinhardt. Isotropic band gaps and freeform waveguides observed in hyperuniform disordered photonic solids. *Proceedings of the National Academy of Sciences*, 110(40):15886–15891, sep 2013.

[15] Weining Man, Marian Florescu, Kazue Matsuyama, Polin Yadak, Geev Nahal, Seyed Hashemizad, Eric Williamson, Paul Steinhardt, Salvatore Torquato, and Paul Chaikin. Photonic band gap in isotropic hyperuniform disordered solids with low dielectric contrast. *Opt. Express*, 21(17):19972–19981, Aug 2013.

[16] O. Leseur, R. Pierrat, and R. Carminati. High-density hyperuniform materials can be transparent. *Optica*, 3(7):763–767, Jul 2016.

[17] Marino Coppolaro, Giuseppe Castaldi, and Vincenzo Galdi. Effects of deterministic disorder at deeply subwavelength scales in multilayered dielectric metamaterials. *Opt. Express*, 28(7):10199–10209, Mar 2020.

[18] Marino Coppolaro, Giuseppe Castaldi, and Vincenzo Galdi. Anomalous light transport induced by deeply subwavelength quasiperiodicity in multilayered dielectric metamaterials. *Phys. Rev. B*, 102:075107, Aug 2020.

[19] S. Torquato, G. Zhang, and F. H. Stillinger. Ensemble theory for stealthy hyperuniform disordered ground states. *Phys. Rev. X*, 5:021020, May 2015.

[20] Robert A. DiStasio, Ge Zhang, Frank H. Stillinger, and Salvatore Torquato. Rational design of stealthy hyperuniform two-phase media with tunable order. *Phys. Rev. E*, 97:023311, Feb 2018.

[21] Eli Chertkov, Robert A. DiStasio, Ge Zhang, Roberto Car, and Salvatore Torquato. Inverse design of disordered stealthy hyperuniform spin chains. *Phys. Rev. B*, 93:064201, Feb 2016.

[22] S. Torquato. *Random Heterogeneous Materials: Microstructure and Macroscopic Properties*. Springer, 2002.

[23] Michael A. Klatt, Jaeuk Kim, and Salvatore Torquato. Cloaking the underlying long-range order of randomly perturbed lattices. *Phys. Rev. E*, 101:032118, Mar 2020.

[24] Jiaju Wu, Feng Wu, Keqiang Lv, Zhiwei Guo, Haitao Jiang, Yong Sun, Yunhui Li, and Hong Chen. Giant goos–hänchen shift with a high reflectance assisted by interface states in photonic heterostructures. *Phys. Rev. A*, 101:053838, May 2020.

[25] Weijing Kong, Yu Sun, and Yu Lu. Enhanced goos-hänchen shift of graphene coated on one-dimensional photonic crystal. *Results in Physics*, 17:103107, 2020.

[26] Xiaodong Du and Haixia Da. Large and controlled goos–hänchen shift in monolayer graphene covered multilayer photonic crystals grating. *Optics Communications*, 483:126606, 2021.

[27] Dong Zhao, Shaolin Ke, Qingjie Liu, Bing Wang, and Peixiang Lu. Giant goos–hänchen shifts in non-hermitian dielectric multilayers incorporated with graphene. *Opt. Express*, 26(3):2817–2828, Feb 2018.

[28] Zihao Liu, Fangyuan Lu, Leyong Jiang, Wei Lin, and Zhiwei Zheng. Tunable goos-hänchen shift surface plasmon resonance sensor based on graphene-hbn heterostructure. *Biosensors*, 11(6), 2021.

[29] Mingyu Mao, Tao Zhang, Sijia Guo, and Haifeng Zhang. Goos–hänchen shift produced by a one-dimensional photonic crystal doped with insb. *J. Opt. Soc. Am. B*, 37(7):2095–2103, Jul 2020.

[30] Hanan Herzig Sheinfux, Ido Kaminer, Yonatan Plotnik, Guy Bartal, and Mordechai Segev. Subwavelength multilayer dielectrics: Ultrasensitive transmission and breakdown of effective-medium theory. *Phys. Rev. Lett.*, 113:243901, Dec 2014.

[31] K. Yu. Bliokh and V. D. Freilikher. Localization of transverse waves in randomly layered media at oblique incidence. *Phys. Rev. B*, 70:245121, Dec 2004.

[32] Kihong Kim. Exact localization length for s-polarized electromagnetic waves incident at the critical angle on a randomly-stratified dielectric medium. *Opt. Express*, 25(23):28752–28763, Nov 2017.

[33] Jan W. Kantelhardt, Richard Berkovits, Shlomo Havlin, and Armin Bunde. Are the phases in the anderson model long-range correlated? *Physica A: Statistical Mechanics and its Applications*, 266(1):461–464, 1999.

[34] J M Luck. Non-monotonic disorder-induced enhanced tunnelling. *Journal of Physics A: Mathematical and General*, 37(1):259–271, dec 2003.

[35] Kurt Artmann. Berechnung der seitenversetzung des totalreflektierten strahles. *Annalen der Physik*, 437(1-2):87–102, 1948.

[36] Marcel Filoche and Svitlana Mayboroda. Universal mechanism for anderson and weak localization. *Proceedings of the National Academy of Sciences*, 109(37):14761–14766, 2012.

# 초 록

무질서한 매질에서의 파동 현상은 Anderson 이 무질서한 결정 구조에서 파동 확산의 부재를 발견한 후 큰 관심을 받아왔습니다. 무질서를 응용한 광학분야에서 최근 연구는 극소 단위 구조의 파동 국부화 및 확산과 무질서한 매질에서 파동 전달과 연관된 제어가능한 상관 길이에 중점을 두고 있습니다. 교란된 질서 구조를 가진 시스템에서 파동-무질서 상호 작용의 결과와 제어가능한 극소 단위 상호작용 및 일반적으로 얻을 수 없는 광학적 특성을 얻은 결과를 무질서 설계를 통해 얻을 수 있었습니다. 따라서 적절한 구조적 상관 관계 조절을 통해 분광 응답 특성, 파동 전달 및 국부화, 각도 응답 및 위상 특성과 같은 여러 물리 량을 제어할 수 있으므로 무질서 엔지니어링이 필수적이라고 할 수 있습니다.

무질서를 구성하는 단위와 관련하여 흥미로운 최근 성과는 축적된 구스-한센 위상 변이에 의해 유도된 강력한 국부화의 출현에 있으며, 이는 유효 매질 이론의 붕괴를 초래하고 임계각에서 비정상적인 투과 현상의 발현을 이끌어냅니다. 그러나 구스-한센 위상 축적의 물리적 현상, 공간 차수 메트

릭 및 파동 현상 간의 연결에 대한 더 깊은 이해는 여전히 존재하지 않아 설계 목적이 분명한 극소 단위 무질서 구조의 역 설계와 같은 더 높은 수준의 추상적인 응용이 이루어지지 않고 있습니다.

이 논문에서는 목표하는 메트릭 $\tau$ 값으로 설계된 초 극소단위 무질서 평면 다층 필름을 보이고, 메트릭 $\tau$ 와 무질서로 인해 유발된 비정상적인 투과 및 국부화 길이의 변화 사이의 상관 관계를 보이며, 국부화, 파동 전달 및 분광, 각도 응답 특성의 제어의 응용 분야에 무질서 설계를 적용할 수 있음을 증명합니다. 필름의 두께에 적용된 무질서의 분포와 국부화 거점들의 위치 사이의 상관 관계도 논의됩니다. 이러한 국부화 거점들은 추가 파동 전파 경로를 생성하여 향상된 측면 이동인 보조 구스-한센 시프트를 만들어냅니다. 또한 무질서에 대칭을 적용하여 투과 시프트를 처음으로 발견했습니다.

본 논문은 파동-무질서 상호작용에 대한 더 깊은 이해를 제공하고 국부화 거점들을 제어하여 임계각 주변의 비정상적인 광학 특성을 제어하는 유망한 무질서 설계 응용 방법을 제공합니다. 중점적으로 볼 것은, 보조 구스-한센 시프트 및 투과 시프트의 출현과 이들의 향상을 통해 각도 필터 및 센서의 잠재적 응용에 대한 새로운 관점을 제안한다는 것입니다.

**주요어**: 무질서 설계, 극소영역 무질서, 무질서 기인 국부화 조절, 국부화 중심, 보조 구스-한센 시프트, 투과 시프트

**학번**: 2018-37775